



Atmospheric data support a multi-decadal shift in the global methane budget towards natural tropical emissions

Alice Drinkwater^{1,2}, Paul I. Palmer^{1,3}, Liang Feng^{1,3}, Tim Arnold^{1,2}, Xin Lan^{4,5}, Sylvia E. Michel⁶, Robert Parker^{7,8}, and Hartmut Boesch^{7,8}

¹School of GeoSciences, University of Edinburgh, Edinburgh, UK

²National Physical Laboratory, Teddington, UK

³National Centre for Earth Observation, University of Edinburgh, Edinburgh, UK

⁴Cooperative Institute for Research in Environmental Sciences, University of Colorado Boulder, Boulder, CO, USA

⁵Global Monitoring Laboratory, National Oceanic and Atmospheric Administration, Boulder, CO, USA

⁶Institute of Arctic and Alpine Research, University of Colorado Boulder, Boulder, CO, USA

⁷National Centre for Earth Observation, Space Park Leicester, University of Leicester, UK

⁸Earth Observation Science, School of Physics and Astronomy, University of Leicester, UK

Correspondence: Alice Drinkwater (alice.drinkwater@ed.ac.uk)

Abstract. We use the GEOS-Chem global 3-D model and a Maximum *A Posteriori* inverse method to infer regional methane emissions and the corresponding carbon stable isotope source signatures, 2004–2020, across the globe using *in situ* and satellite remote sensing data. Over our study period, we find consistent evidence from both atmospheric CH₄ datasets of a progressive increase of methane emissions at tropical (30°N to 30 °S) latitudes (+3.80 Tg/yr/yr), accompanied by a progressively lighter atmospheric δ¹³C signature, consistent with increasing natural emissions. The satellite remote sensing data provide evidence of higher spatially resolved hotspots of methane that are consistent with the location and seasonal timing of wetland emissions, limiting the hypothesis about the hydroxyl radical (OH) sink for methane playing a significant role in observed global growth in atmospheric methane. We find that since 2004, the largest growing regional contributions (2004–2020) are from North Africa (+19.9 Tg/yr), China (+21.6 Tg/yr), and Tropical South America (+14.2 Tg/yr). To quantify the influence of our results to changes in OH, we also report regional emission estimates using an alternative scenario of a 0.5%/yr decrease in OH since 2004, followed by a 5 % drop in 2020 during the first COVID-19 lockdown. We find that our main findings are robust against those year-to-year changes in OH.

1 Introduction

Changes in atmospheric methane (CH₄) over the last decades have unfolded without clear explanation, exposing inadequacies in our measurement coverage and our ability to definitively attribute those changes to individual emissions and losses. The climatic importance of atmospheric CH₄ lies in its ability to absorb and emit infrared radiation, at wavelengths that are relevant to outgoing terrestrial radiation. Consequently, atmospheric CH₄ helps to maintain Earth's radiative balance and surface and atmospheric temperatures. Concentrations of atmospheric CH₄ are determined by a large range of anthropogenic, pyrogenic, and biogenic emissions and losses from the hydroxyl radical (OH), reaction with chlorine, uptake from soils, and a small



20 stratospheric loss. The global CH₄ growth rate was close to zero from 2000 to 2006 (Dlugokencky et al., 2020) but has since
accelerated to unprecedented values in 2020 and 2021 (Feng et al., 2022a). Concurrently, we are witnessing progressively
lighter CH₄ (more negative δ¹³C), indicative of a higher proportion of microbial emissions. A growing body of work have
proposed a range of hypotheses to explain short periods of observed global and regional variations in atmospheric CH₄ (Turner
et al., 2019). In this study, we take a step back to look at observed CH₄ variations from 2004 onwards, and argue that short-term
25 variations are part of a large-scale shift of predominately anthropogenic emissions from high northern latitudes to microbial
emissions from the tropics, driven by Tropical North African and Tropical South American wetlands. As the global atmospheric
mass balance of CH₄ emissions shifts further from anthropogenic to microbial sources, our ability to mitigate emissions
becomes more of a challenge.

The post-2006 increase in atmospheric CH₄ has been the focus of many studies and has been attributed to different plausible
30 hypotheses associated with changes in fossil fuel, biomass burning, and wetland emissions and the OH sink (Turner et al.,
2019). These studies have reached their conclusions using *in situ* mole fraction observations alone or in combination with
other observations, e.g. *in situ* δ¹³C (Schaefer et al., 2016; Rice et al., 2016; Nisbet et al., 2016; Fujita et al., 2020; Lan et al.,
2021), satellite observations (Worden et al., 2017; McNorton et al., 2018; Yin et al., 2021; Feng et al., 2022b), or other trace
gases, using a variety of analysis methods and computational models. Our approach is unique in that, for our δ¹³C inversion, we
35 are solving for the δ¹³C source signature of a region. From the source signature of a region, we can determine how the source
balance within a region is shifting over time (i.e., towards more pyrogenic or microbial sources), and so gain understanding of
the geographical shifts in the CH₄ budget.

Changes in OH are likely to play some role in recent changes in atmospheric CH₄ (Rigby et al., 2017; Turner et al., 2017)
but they are unlikely to be a dominant factor. Lan et al. (2021) simulated CH₄ and δ¹³C in a 3-D chemistry transport model
40 covering the period 1984-2016, and found that proposed changes in OH (by Turner et al., 2017) do not align with the trend
of increasingly light δ¹³C observed in the atmospheric record, due to the weak fractionation of OH. We explore the impact
of reducing OH in a sensitivity study. The first COVID-19 lockdown in 2020 corresponded to an unexpected large increase in
atmospheric CH₄. Studies have suggested this could be partly explained by a 3-5 % reduction in OH (Miyazaki et al., 2021;
Laughner et al., 2021) resulting from a large-scale reduced emissions of nitrogen oxides associated with industry. This has yet
45 to be corroborated by satellite data that provide complementary constraints on the key emitting regions over the tropics (Feng
et al., 2022b), or by δ¹³C data.

In the next section, we describe the data and methods we use to quantify changes in CH₄ emissions and the corresponding
stable isotope source signatures. In section 3, we report our results including analysis of sensitivity calculations that involve
different assumptions about year to year changes in the OH sink. We conclude the paper in section 4.



50 2 Data and Methods

2.1 *In Situ* and Satellite Remote Measurements of Atmospheric Methane

We use surface-level flask data as constraints on both total CH₄ emissions and δ¹³C regional emissions source signatures. These data are taken from 31 National Oceanic and Atmosphere Administration — Global Monitoring Laboratory (NOAA-GML) sites around the world (Figure 1), version 2020-07 (Dlugokencky et al., 2020). The data are monthly mean values, averaged
55 from discrete data as collected at each site, analysed at NOAA-ESRL in Boulder, Colorado, and recorded to the NOAA 2004A standard scale (Dlugokencky et al., 2005). Up to August 2019, the analysis was performed using gas chromatography (Steele et al., 1987, Dlugokencky et al., 1994; Dlugokencky et al., 2005) and since August 2019, cavity ringdown spectroscopy has been used (Dlugokencky et al., 2020). We also include data from a site in Siberia, Karasevov (KRS), which is monitored by the National Institute for Environment Studies (NIES). This site was included to maximise geographical coverage of *in situ* data.
60 The CH₄ measurements from this site are continuous, measuring from 65 m height, covering the period 2004-2020 (Sasakawa et al., 2010). A scale factor of 0.997 is applied to the NIES data in order to bring it into line with the NOAA 2004A scale (Zhou et al., 2009). The site constitutes part of the Japan-Russia Siberia Tall Tower Inland Observation Network (JR-STATION).

δ¹³C data are similarly monthly mean values, calculated from discrete flask samples at NOAA network sites. Isotopic analysis of δ¹³C was performed at the University of Colorado Institute of Arctic and Alpine Research Stable Isotope Laboratory
65 (CU-INSTAAR). They follow an isotope ratio mass spectrometry approach (Miller, 2002; Vaughn et al., 2004). The geographical locations of *in situ* data used are shown in Figure 1 and represent a subset of those used to collect total CH₄ amount fractions (10 of 32). The sites included in the inversion, both for CH₄ and δ¹³C are those that cover the entire period of the inversion (2004-2020) without significant period of measurement breaks so as to ensure a consistent interpretation of trends without consideration of possible biases introduced through the inclusion or exclusion of specific sites.

70 We also estimate CH₄ fluxes for 2010-2020 from the Japanese Greenhouse gases Observing SATellite (GOSAT) that was launched in 2009. GOSAT is in a sun-synchronous orbit with an equatorial local overpass time of 13:30. Since launch, it has provided continuous global observations of dry-air atmospheric column-averaged carbon dioxide CO₂ (XCO₂) and CH₄ (XCH₄), retrieved from shortwave infrared wavelengths that are most sensitive to changes in CH₄ and CO₂ in the lower troposphere (Parker et al., 2020). We use the latest (v9) proxy XCH₄:XCO₂ retrievals that use spectral absorption features
75 around the wavelength of 1.6 μm (Parker et al., 2020, Palmer et al., 2021), because of the smaller bias and better global coverage than those provided by the full physics retrievals. Analysis shows the precision of single proxy retrieval is about 0.72 %, with a global bias of 0.2 % (Parker et al., 2011, 2015, 2020). In our calculations, we assume a higher observation uncertainty of 1.2 %, and deduct a globally uniform bias of 0.3 % to obtain better *a posteriori* agreement with the independent ground-based XCH₄ data by the Total Carbon Column Observing Network (TCCON). To anchor the constraints from the
80 proxy XCH₄:XCO₂ ratio (Fraser et al., 2014; Feng et al., 2017), we also assimilate the GLOBALVIEW CH₄ and CO₂ data (Schuldt et al., 2021), with assumed uncertainties of 0.5 ppm and 8 ppb for *in situ* measurements of CO₂ and CH₄, respectively. Locations of the assimilated GLOBALVIEW CH₄ (sub) dataset are shown in Feng et al., 2022b.



2.2 GEOS-Chem Atmospheric Chemistry and Transport Model

To relate CH₄ emissions to atmospheric CH₄ concentrations, we use v12.1 of the GEOS-Chem 3-D global chemical transport
85 model (CTM) (Bey et al., 2001) at a horizontal resolution of 2° (latitude) by 2.5° (longitude) with 47 vertical levels from
the surface to 80 km height, driven by the MERRA-2 meteorological reanalyses (Gelaro et al., 2017) from the NASA Global
Modeling and Assimilation Office (GMAO).

Our *a priori* emissions include: 1) monthly EDGAR 4.3.2 anthropogenic emissions (Source: European Commission, 2011)
that accounts for emissions from oil and gas, coal, livestock, landfills, wastewater, rice, and other anthropogenic sources; 2)
90 monthly GFED-4 biomass burning emissions (version 4.1; Randerson et al., 2017); and 3) monthly v1.0 WetCHARTs wetland
emissions (Bloom et al., 2017). The Harvard-NASA Emissions Component (HEMCO) software within GEOS-Chem converts
the emission inventories at their native horizontal resolution to the GEOS-Chem 2° × 2.5° resolution.

Table 1 shows the δ¹³C signatures for the source types included in our simulations. These are extracted as mean global
values from Sherwood et al. (2017), which provides a database of global source signatures, broken down into the same sectors
95 as we employed in our simulations. However, individual source types show a wide range of source signatures (e.g., coal mines
(Zazzeri et al., 2016)), and this uncertainty is reflected in the assigned uncertainty given to the *a priori* source signatures in
inversion (Section 2.3). We differentiate between Arctic and tropical wetlands by applying a 10 % lighter source signature
to the Arctic source (Table 1), following Ganesan et al. (2018) who produced a global wetland source signature map based
upon published δ¹³C data. The arithmetic underlying the conversion of isotope ratios to isotopologue emissions for input to
100 the model are detailed in Appendix A.

We include the loss of atmospheric CH₄ from reaction with chlorine, soil uptake, and from oxidation by OH. We use
monthly 3-D fields of OH, calculated using the full-chemistry version of GEOS-Chem, and monthly 3-D field of atomic
chlorine ((Sherwen et al., 2016)). Stratospheric loss frequency fields are determined using the NASA GMI stratospheric model
(Duncan et al., 2007). Estimates of the microbial consumption of CH₄ in soils is determined from Fung et al. (1991). The
105 resulting atmospheric lifetime of CH₄ against OH is 9.73 years, consistent with the observed methyl chloroform lifetime of
5.39 years. In our default model configuration, none of these loss processes include interannual variations.

To account for isotopic fractionation due to loss of CH₄ in the troposphere and stratosphere, we use published kinetic
isotope effect values (KIEs). These values are employed to scale the reaction rate constants used in the simulations for ¹²CH₄
and ¹³CH₄ (Table 2). The OH and Cl sinks are handled in the hard coding of the model, whereas the soil sink is handled as a
110 negative emission in the HEMCO file. Therefore, for the soil sink, the KIE is directly applied as a scale factor in the HEMCO
configuration file (Snover and Quay, 2000; Burkholder et al., 2019).

‘Spinning up’ is an important aspect of atmospheric modelling in order for simulated mole fractions to reach equilibrium. We
spin-up the model by scaling a CH₄ restart file from an older, coarser resolution GEOS-Chem model run. The δ¹³C inversion
uses *a posteriori* regional emissions from the CH₄ inversion as a starting point, with sectoral emissions scaled as detailed in
115 Appendix A. We then run the model over the year 2004 sixty times using the 2004 MERRA-2 meteorology and emissions,
corresponding to approximately six times the chemical lifetime of CH₄. We find this is sufficient to allow mole fractions and



isotope ratios to equilibrate (not shown). We then run a single-year inversion for 2004 to optimise the $\delta^{13}\text{C}$ and total CH_4 values relative to NOAA observations, following inverse method detailed below. The output of this short inversion is improved estimates of initial conditions for $\delta^{13}\text{C}$ and total CH_4 , which serve as a starting point for the longer inversion we report here (2004-2020).

For all our calculations, we sample GEOS-Chem at the grid square and local time that corresponds to the *in situ* and satellite remote sensing data. For the satellite data, we also apply scene-dependent averaging kernels to account for vertical structure. This approach allows us to directly compare the model with measurements. Regional trends are calculated by examining the grid squares which correspond with a given region on the global grid.

2.3 Inverse Methods

We use two inverse methods that reflect the volume and simplicity of the data being used. For *in situ* data we use the Maximum *A Posteriori* (MAP) inverse methods and for the more voluminous satellite data we use an ensemble Kalman filter. For brevity, we include only the essential details about either method and refer the reader to dedicated papers.

2.3.1 Maximum *A Posteriori*

To infer regional *a posteriori* CH_4 fluxes and regional $\delta^{13}\text{C}$ emissions source signatures from the atmospheric measurements of CH_4 , we use the Maximum *A Posteriori* solution (MAP) inverse method. We solve for fluxes and $\delta^{13}\text{C}$ emissions signatures from 14 geographical regions (Figure 1). This method combines *a priori* knowledge and its uncertainty with the measurements and their uncertainties, and has been used in a number of studies, e.g., Fraser et al. (2014); McNorton et al. (2018).

The MAP solution and the associated *a posteriori* uncertainty is described as, using the conventional that lower-case and upper-case variables denote vectors and matrices, respectively:

$$\mathbf{x}^a = \mathbf{x}^b + (\mathbf{H}^T \mathbf{B}^{-1} \mathbf{H} + \mathbf{R}^{-1})^{-1} \mathbf{H}^T \mathbf{B}^{-1} (\mathbf{y} - \mathbf{H} \mathbf{x}^b), \quad (1)$$

$$\mathbf{A} = (\mathbf{H}^T \mathbf{B}^{-1} \mathbf{H} + \mathbf{R}^{-1})^{-1}, \quad (2)$$

where \mathbf{x} denotes the state vector that describes the estimated quantities, which in this study includes monthly CH_4 fluxes and $\delta^{13}\text{C}$ source signatures from regions across the world (Figure 1). Subscripts ‘a’ and ‘b’ denote *a posteriori* and *a priori* fluxes, respectively, and superscripts ‘-1’ and ‘T’ denote matrix inverse and transpose operations, respectively. The measurement vector \mathbf{y} includes either NOAA mole fraction data and the $\delta^{13}\text{C}$ data. The matrices \mathbf{B} , \mathbf{A} , and \mathbf{R} denote the error covariances matrices for the *a priori*, *a posteriori*, and measurements, respectively. \mathbf{B} and \mathbf{R} are diagonal matrices. For \mathbf{B} we assume uncertainties of 50 % of the regional CH_4 fluxes and 15 % for the $\delta^{13}\text{C}$ values, and for \mathbf{R} we assume 10 ppb for the mole fraction data and 0.1 % for the isotope data. We assume a model transport error of 12 ppb, following Feng et al. (2022b).

The Jacobian matrix \mathbf{H} describes the sensitivity of the measurements to changes in the state vector, i.e. $\partial \mathbf{y} / \partial \mathbf{x}$. For the total CH_4 inversion, the Jacobian matrix describes the sensitivity of mole fractions in the model to changes in regional CH_4 emissions. We construct the matrix using a series of GEOS-Chem model runs. We systematically let each individual emitting region (described by the state vector) emit for one month while all other regions are emitting as normal. The individual regional



source is then switched off (emissions set to zero) and the effect of this on the 3-D atmospheric distribution of CH₄ mole
150 fractions is recorded over the following three months. The result of this test is recorded at the grid squares that correspond
with the measurement sites. The resulting mole fractions therefore describe the sensitivity of a particular measurement site to
changes in a specific regional source up to three months after emission. This is repeated for every month within the inversion
timescale, for every region described in the state vector.

For the $\delta^{13}\text{C}$ inversions, the *a priori* simulation uses *a posteriori* regional emissions from the CH₄ inversion as a starting
155 point. The Jacobian matrix in this case describes the sensitivity of modelled $\delta^{13}\text{C}$ to changes in the regional source signatures.
We construct the Jacobian as the difference between a control model calculation (using the CH₄ *a posteriori* regional emissions)
and perturbed source signature model calculation for the whole study period (2004-2020). For the perturbed model calculation,
we systematically perturb the source signature of each region (all of the sectors that are containing geographically within a
region) so that it is heavier by 20 ‰ for the period 2004-2020. The difference between the control and perturbed run in $\delta^{13}\text{C}$
160 value at the location of each measurement site is then divided by the ‰ value of $\delta^{13}\text{C}$ perturbation for the region source
signature, to understand the effect of changing a regions source signature upon the $\delta^{13}\text{C}$ value recorded at each measurement
site location. Each individual regions' model calculation is spun up separately from the control model calculation in order to
account for lagging in the model.

The output from the inversion are improved estimates of regional fluxes and $\delta^{13}\text{C}$ source signatures. The model simulates
165 the global atmosphere on a $2^\circ \times 2.5^\circ$ grid. The *a posteriori* regional fluxes and source signatures are applied to the grid squares
in the model which correspond with a given region in an *a posteriori* simulation.

2.3.2 Ensemble Kalman Filter

We use an Ensemble Kalman Filter (EnKF) approach in performing the inversion using satellite data, because we cannot easily
evaluate the necessary matrix operations associated with an analytic inversion. Here we use an ensemble of flux perturbation
170 pulses to represent uncertainty in our *a priori* estimate for regional monthly fluxes. We subsequently use a global chemistry
transport model (i.e., the GEOS-Chem v12) to track the transport and chemistry processes of the tagged emission pulses in
the atmosphere, to project their spreads to the observation space. With the ensemble of *a priori* flux perturbations, and the
simulated observation impacts, we use the Ensemble Transform Kalman Filter (ETKF) algorithm to numerically estimate the
a posteriori fluxes and the associated uncertainties by optimally comparing the model simulation with observations (see Feng
175 et al., 2017 for more details). To reduce the computational costs, mainly from tracking tagged emission pulses, we introduce
a 4-month moving lag window for each assimilation step, because any observation has limited ability to distinguish between
the signals emitted long (>4 months) before, from variations in the ambient background atmosphere (Feng et al., 2017). As
a result, we are able to include a larger state vector, consisting of monthly scaling factors for 487 (476 land regions and
11 oceanic regions) regional CH₄ (and CO₂) pulse-like basis functions (Figure S1 in (Feng et al., 2022b)). We define these
180 land sub-regions by dividing the 11 TransCom-3 (Gurney et al., 2002) land regions into 42 to 56 nearly equal sub-regions,
and use the 11 oceanic regions defined by the TransCom-3 experiment. Because of their smaller sizes, we have assumed a



higher uncertainty percentage (60 %) for *a priori* emissions than the MAP approach described above. We also include spatial correlation with a correlation length of 500km between the sub-regions.

3 Results

185 Figure 2 shows the regional differences between *a priori* and *a posteriori* emission estimates, with absolute emissions values plotted in Figure A1. Here we show the annual mean difference between the *a posteriori* and the *a priori* emissions, for both NOAA and GOSAT inversion results. This indicates the changes from the *a priori* emissions and allows comparison of the two independent approaches. The *a priori* emissions are constructed as detailed in Section 2.2. At a global scale, we find increased emissions relative to *a priori* emissions of 72.0 ± 35.51 Tg/yr in 2020 for the *in situ* inversion and 61.5 ± 37.3 Tg/yr higher emissions for the GOSAT inversion. The *in situ* inversion results indicate that this difference originates from 190 tropical regions such as Tropical South America ($+13.5 \pm 1.9$ Tg/yr in 2020), North Africa ($+15.1 \pm 6.8$ Tg/yr, 2020) and China ($+17.3 \pm 4.4$ Tg/yr, 2020). There are decreases relative to *a priori* emissions in 2020 in Temperate North America (-13.3 ± 3.4 Tg/yr), Southern Africa (-5.6 ± 2.1 Tg/yr), Temperate South America (-4.1 ± 4.0 Tg/yr) and Boreal Eurasia (-2.3 ± 3.9 Tg/yr). Therefore, the estimates from bottom up inventories underestimate CH₄ emissions, especially in tropical regions. According 195 to these results, mid-litudinal emissions are being overestimated and tropical emissions underestimated.

Likewise, the GOSAT-based inversion results indicate *a posteriori* emissions increases from the *a priori* emissions are centred around tropical regions. In 2020, there are emissions increases from the *a priori* estimates in Tropical South America ($+20.3 \pm 1.9$ Tg/yr) and North Africa ($+13.1 \pm 6.8$ Tg/yr). Similar to the *in situ* results, there are decreases in some mid-litudinal regions, specifically Temperate North America (-3.9 ± 1.8 Tg/yr) and Temperate South America (-6.4 ± 7.1 Tg/yr).

200 The increase in tropical emissions has been highlighted by previous studies, whether using GOSAT data or *in situ* data as constraints in a 3-D CTM inversion (McNorton et al., 2016 and Fujita et al., 2020, examining (2003-2015) and (1995-2013) respectively). The increase in North Africa is especially noteworthy in 2020, where emissions have been attributed to increased wetland emissions by previous studies (Lunt et al., 2019, 2021; Pandey et al., 2021; Feng et al., 2022b).

There are some differences between the two inversion results. Specifically, emissions from Boreal North America and China 205 are lower than the *a priori* emissions for the GOSAT-based inversion (-4.6 ± 1.1 and -5.1 ± 3.8 Tg/yr in 2020 respectively), but increase for the *in situ* inversion ($+4.4 \pm 3.$ and $+17.3 \pm 4.4$ Tg/yr in 2020 respectively). It is noteworthy that, despite differences in the absolute annual emissions estimates, both the GOSAT-based inversion and the *in situ* based inversion indicate a gradual emissions increase in China from 2012. Sheng et al. (2021) find anthropogenic CH₄ emissions from China increasing by 0.36 Tg/yr, from 2012 to 2017 using GOSAT data. Comparing the same time period, we find an increase of Chinese emissions of 210 0.72 Tg/yr inferred from the ground-based *in situ* data and increase of 1.34 Tg/yr inferred from the GOSAT data.

Figure A4 shows mole fraction estimates and *a posteriori* mole fraction estimates inferred from the NOAA surface data at site locations. We find smaller residuals between simulated mole fractions using the *a posteriori* emissions and the measurements (mean residual 9.01 ppb; root-mean-square error (RMSE) 11.94 ppb) than between the *a priori* values and the measurements (mean residual 13.06 ppb; RMSE 17.13 ppb). This compares favourably with studies such as McNorton et al. (2018), with



215 *a posteriori* RMSE of 12.30 ppb. Likewise, we see agreement of mole fraction estimates using GOSAT data (Figure A5; mean residual 41.72 ppb, RMSE 51.57 ppb). There are no significant *a posteriori* correlations between neighbouring regions (Figure A6), determined by the *a posteriori* error covariance matrix, **A**, meaning that the *a posteriori* regional emissions estimates are independent of one another.

Figure A7 shows the monthly regional source signature values for *a priori* and *a posteriori* simulations. General observations from this figure are that lighter signatures are observed (-62‰) from Northern Boreal regions (Boreal North America and Eurasia), which indicates the dominance of biogenic emissions here. Conversely, we observe heavier source signatures (-40‰ , indicative of a greater proportion of anthropogenic emissions) from regions such as Temperate Eurasia, Australia and Southern Africa. Some regional $\delta^{13}\text{C}$ source signatures have a much stronger seasonal cycle than others (strongest in Boreal North America and Boreal Eurasia but also in Northern and Southern Africa), with lighter values during summer months, driven by a greater proportion of biogenic emissions at this time. It therefore follows that less significant seasonality is indicative of anthropogenic emissions making up a significant part of the emissions mix (observed for example in China and Temperate Eurasia). Tropical Asia shows a yearly cycle with dual peaks, which is due to a combination of wetland and rice emissions. This assessment assumes that sources are playing the most significant role in controlling seasonal cycle in $\delta^{13}\text{C}$ source signature, although we do not discount a role for changes in the loss processes.

230 Figure 3 shows *a posteriori* regional $\delta^{13}\text{C}$ emissions source signatures inferred from ground-based *in situ* data. The results are grouped into approximately three-year bands, as a residual from the 2004-2007 mean value, to show how the source signatures change across the time series. There is a general trend towards lighter regional source signatures of $\delta^{13}\text{C}$ across the time series. This trend has been ongoing since 2012 and is observed in all regions worldwide, however is strongest as compared with *a priori* estimates in Tropical and Southern Hemispheric regions such as Tropical South America and Southern Africa (1.8 ‰ and 2.1 ‰ lighter than *a priori* for 2019-2020, respectively). There is also evidence to suggest a period around 2012 when regional source signatures become heavier (by approximately 1.0 ‰ compared with *a priori* source signatures), especially in the Northern Hemisphere, before becoming lighter again. The heavy trend is dominant in the Northern Hemisphere, suggesting a larger proportion of anthropogenic emissions in this region at this time. This heavy shift around 2008 and light shift in 2012 is also noted by Nisbet et al. (2016), who use a box model and examine data from sites measured by NOAA and Royal Holloway, University of London (RHUL). They found that changes in removal rates would not explain these anomalies; the events are therefore attributed to changing emissions. Emissions growth post-2012 aligns with our atmospheric growth rates plotted in Figures A2, A1.

245 We find some significant *a posteriori* correlations between neighbouring regions for these source signatures (Figure A8), determined by the *a posteriori* error covariance matrix, **A**, which indicates that we cannot differentiate between the source signatures of neighbouring regions (such as Southern Africa and Temperate South America). Nevertheless, the trend of stronger emissions of lighter CH_4 is clear, indicating an increased role in biogenic or wetland emissions in the global source makeup. Lan et al. (2021) corroborate this using a 3-D chemical transport model to simulate different possible emissions scenarios, and find that microbial emissions (wetlands, agriculture and waste) are responsible for increasingly light $\delta^{13}\text{C}$ signature, examining 1984-2016.



250 The corresponding *a posteriori* regional $\delta^{13}\text{C}$ source signatures produce an atmospheric time series more consistent with measurements than *a priori* values (Figure A9), particularly during 2008-2018 when *a priori* values result in significantly lighter emissions source signatures. Figure A9 shows $\delta^{13}\text{C}$ *a priori* and *a posteriori* values at site locations. The *a posteriori* source signatures result in smaller residuals between the *a posteriori* simulation and measurement (mean residual 0.11 ‰, RMSE 0.15 ‰), than from the prior (mean residual 0.19 ‰, RMSE 0.23 ‰). These compare well to McNorton et al. (2018) 255 (*a posteriori* RMSE 0.1 ‰) and Fujita et al. (2020) (*a posteriori* RMSE 0.08 - 0.25 ‰).

In Figure 4, we combine this information into a zonal plot, reported approximately every 30° latitude, for CH₄ emissions and the corresponding changes in regional source signatures of $\delta^{13}\text{C}$. We find consistency between the magnitude of the changes in CH₄ inferred from NOAA and GOSAT data, particularly in the low latitudes. The plot also shows there has been a progressive increase in emissions from tropical latitudes (between 60-80 Tg/yr in 2019-2020) and a decrease at northern midlatitudes (up 260 to -10 Tg/yr). This suggests that emissions have shifted from northern midlatitudes towards tropical emissions. We also find a move towards lighter regional source signatures of $\delta^{13}\text{C}$ across all latitudinal bands, with a change of approximately -2 ‰ in the tropics. Comparing Figures 3 and 4, we see similar trends across latitudinal bands and the regions within them, for example trends in European and Chinese source signatures align with the 30-60° N latitudinal band. Our results compare well with Nisbet et al. (2019), who use a box model to fit emissions scenarios to *in situ* measurements, examining 2000-2018. They show 265 strongest emissions increases from the tropics (approximately + 20 Tg/yr, Figure 5). They likewise show consistently lighter $\delta^{13}\text{C}$ across the time series of $\delta^{13}\text{C}$ by approximately 0.5 ‰/yr.

Figure A2 compares our calculated atmospheric growth rate from the model simulations with the growth rates calculated from the *in situ* observations alone. We applied the same technique as NOAA follow to compare their published growth rate to the *a posteriori* mole fractions of our inversion. The general trend in increasing growth rate is evident in both measurement 270 and model datasets with inter-annual discrepancies explained through model measurement mismatch at specific sites.

To examine the sensitivity of our results to changes in OH, we run a single sensitivity run that is made up of two parts. First, we imposed a 0.5 ‰/yr uniform decrease to our 3-D OH field from 2004 to 2019, following similar trends proposed by Turner et al. (2017) (who proposed a 7 % reduction in OH, 2003-2016) and second, we uniformly decrease OH by 5 % in 2020 to describe estimated changes due to a global-scale reduction in emissions of nitrogen oxides (NO_x) associated with 275 the first COVID-19 lockdown Miyazaki et al. (2021); Laughner et al. (2021). It has also been suggested that OH levels may have actually increased during 2000–2016 due to increasing water vapour and NO_x in the tropics (Zhao et al., 2019), however considering the scenario under COVID-19 lockdowns in 2020, a decreasing trend over the previous years is only considered here. A similar approach to this was followed by Feng et al. (2022b) for which there is some opposition that suggests the change in OH during COVID-19 should be larger although there is no empirical determination of this change. We then recalculate 280 *a posteriori* emissions inferred from the *in situ* NOAA data. Figure A3 shows that the 0.5 ‰ negative trend in OH does not make a significant difference to our *a posteriori* estimates (emissions change is not larger than a *a posteriori* uncertainty) until later in the timeseries (2017-2019), reflecting our large *a posteriori* uncertainties. However, we find that a sudden 5 % decrease in OH during 2020 results in a marked reduction (approximately 9 %, 50 Tg/yr) in the increased emissions necessary to explain the increase in atmospheric CH₄. This reduction in necessary increases in emissions particular affects high-emitting regions



285 such as China and Tropical Asia. Despite this, the regional results are generally within the *a posteriori* uncertainties of our control calculation, which does not include a year-to-year change in OH. On balance, given the large-scale, unprecedented changes in atmospheric chemistry during 2020 it is likely that OH has a role to play in the global growth rate of CH₄ but changes in emissions overwhelm the impact from reduced OH. We find a similar fit of the model to data with or without considering the OH trend (not shown).

290 4 Conclusions

We estimated regional CH₄ emissions and $\delta^{13}\text{C}$ source signatures for the period 2004-2020, inclusively, by fitting the GEOS-Chem 3-D atmospheric chemistry transport model to NOAA *in situ* surface mole fraction data and GOSAT atmospheric column data using Bayesian inverse methods. Collectively, our results indicate that the post-2007 increase in CH₄ emissions are best explained by a progressive latitudinal shift in emissions from the northern midlatitudes to tropical latitudes. *A posteriori* CH₄ 295 emission estimates inferred from the NOAA and GOSAT data show larger tropical emissions, particularly over North Africa, Tropical Asia, and Tropical South America, at the same time as mid-latitudinal emission proportion decreases. Source signature estimates inferred from the $\delta^{13}\text{C}$ measurements over the same time period indicate that the latitudinal shift in CH₄ emissions is due to larger proportion of biogenic sources. Our results are broadly consistent with previous studies that focus on shorter, contributing periods (McNorton et al., 2018; Nisbet et al., 2019; Fujita et al., 2020; Yin et al., 2021; Lan et al., 2021)).

300 Our control calculations used monthly 3-D distributions of OH without any year-to-year variation. To explore how changes in OH might affect our results, we ran a sensitivity experiment for which the monthly 3-D OH fields was decreased 0.5 %/yr from 2004 to 2019, inclusively, based on values proposed by previous studies (Turner et al., 2017). For this sensitivity experiment, we find our results are within *a posteriori* uncertainty of the control calculations for most of the time series, and therefore steadily decreasing OH concentrations are not responsible for observed changes in the distribution of CH₄. We also considered 305 how a proposed larger 5% change in 2020 (Miyazaki et al., 2021; Laughner et al., 2021), due to widespread COVID-19 related emission reductions in nitrogen oxides, affected our results. We find smaller CH₄ emissions increases during 2020, as expected, but for most regions they are still within our control *a posteriori* emissions estimates for 2020. A much larger reduction in OH would be necessary to describe exclusively observed changes in atmospheric CH₄, which would consequently affect regional isotope signatures and observed variations of many atmospheric trace gases in a manner that has yet to be reported.

310 Sparse geographic coverage of ground-based data results in larger uncertainties for regional emission estimates that are poorly covered, i.e., high and low latitudes. For CH₄, this deficiency can be partly addressed using the satellite data, but isotopes are not currently retrieved reliably from satellite remote sensing instruments. In this study, there are only three long-term measurement sites for $\delta^{13}\text{C}$ employed in the southern hemisphere. A consequence of this data sparseness is strong correlations between source signatures from neighbouring regions (Figure A8). We further limited our study by picking measurements sites 315 for which data are available over our study period (Figure 1). Sectoral source signatures $\delta^{13}\text{C}$ are taken as mean values from Sherwood et al. (2017), representing our current best knowledge. Different sectors produce a range of possible $\delta^{13}\text{C}$ values, and there are significant overlaps between recorded source signatures (Douglas et al., 2017). These data have greater value when



they are used in a broader context with other data, as we have described in this study. We have used satellite observations to help identify that large-scale emission changes over regions that coincide with wetlands. The collective evidence demonstrates that increasing natural, tropical emissions play a significant role in the observed atmospheric growth of CH₄. Greater confidence in source attribution of changes in atmospheric CH₄ may come from collecting and interpreting δ D and multiply-substituted ‘clumped’ isotopes (Douglas et al., 2017), alongside δ^{13} C. This needs to be accompanied by laboratory and field measurements of these isotopes to improve delineation between different sectors.

Our work is also consistent with recent studies that have reported anomalous large CH₄ emissions over Eastern Africa (East Africa and the Horn of Africa) due to elevated rainfall over upstream catchment areas (Lunt et al., 2019, 2021; Pandey et al., 2021). These large-scale precipitation changes have been linked with the positive phase of the Indian Ocean Dipole (Feng et al., 2022b), which describes a sea-surface temperature gradient over the Indian Ocean. Similarly, increase CH₄ emissions over the Amazon basin (Wilson et al., 2021) are linked with large-scale changes in climate (Feng et al., 2022b). These substantial increases in natural CH₄ emissions will likely have major implications for our achieving the goals of the Paris Agreement (Nisbet et al., 2019). Nature does not care about the origin of atmospheric CH₄ so that increasing natural emissions will require larger emission reductions from anthropogenic sectors, placing additional pressure on citizens to reduce their carbon footprints.

5 Code and data availability

The community-led GEOS-Chem model of atmospheric chemistry and model is maintained centrally by Harvard University (http://geos-chem.seas.harvard.edu), and is available on request. The ensemble Kalman filter code is publicly available as PyOSSE (https://www.nceo.ac.uk/data-tools/atmospheric-tools/).

All the data and materials used in this study are freely available. The NOAA-GML and CU-INSTAAR ground-based CH₄ and δ^{13} C data are available from the NOAA GML FTP server (https://gml.noaa.gov/dv/data), subject to their fair use policies. Data from JR-STATION network was provided with cooperation of NIES Japan. The University of Leicester GOSAT Proxy v9.0 XCH₄ data are available from the Centre for Environmental Data Analysis data repository at (https://doi.org/10.5285/18ef8247f52a4cb6a14013f8235cc1eb), and from the Copernicus Climate Data Store. EDGAR data is available at (https://edgar.jrc.ec.europa.eu/), GFED-4 data is available at (https://www.globalfiredata.org/data.html), WETCHARTS data is available at (https://daac.ornl.gov/cgi-bin/dsviewer.pl?ds_id=1502).

Appendix A: Isotopologue Emissions

To simulate the atmospheric isotope ratio δ^{13} C the isotopologues ¹²CH₄ and ¹³CH₄ are considered separately in the model. To calculate the specific sectoral isotopologue emissions we use the emissions calculated from the total CH₄ simulation and the isotope ratios defined in Table 1. We consider the isotope ¹³C relative to all isotopes in the sample (designated thereafter as



13x) using:

$$13x = \frac{{}^{13}\text{C}}{{}^{12}\text{C} + {}^{13}\text{C}} = \frac{{}^{13}\text{C}/{}^{12}\text{C}}{1 + ({}^{13}\text{C}/{}^{12}\text{C})}, \quad (\text{A1})$$

350 where ${}^{13}\text{C}/{}^{12}\text{C}$ is calculated from the $\delta^{13}\text{C}$ reported on the international carbon isotope scale (VPDB). This is the proportional molar abundance of the isotopologues containing ${}^{13}\text{C}$ (dominated by ${}^{13}\text{CH}_4$). This value has to be adjusted before being applied in GEOS-Chem to convert from isotope ratio values to kg values used by emission inventories:

$$SF13 = 13x \times \frac{M_{13}}{M_{tot}}, \quad (\text{A2})$$

where ‘SF13’ is the scale factor applied to each emissions type for the ${}^{13}\text{CH}_4$ simulation, M_{13} is the molecular weight of ${}^{13}\text{CH}_4$ (17.035 g/mol) and M_{tot} is the molecular weight of CH_4 (16.04 g/mol).

For the ${}^{12}\text{CH}_4$ counterpart to ${}^{13}\text{CH}_4$, we use a similar approach. The ratio of ${}^{12}\text{C}$ compared with all isotopes in the sample (designated as 12x) is given by:

$$12x = \frac{{}^{12}\text{C}}{{}^{13}\text{C} + {}^{12}\text{C}}. \quad (\text{A3})$$

This is similarly adjusted from molar to mass ratio; ‘SF12’ is the scale factor for each emissions type in the ${}^{12}\text{CH}_4$ simulations:

$$SF12 = 12x \times \frac{M_{12}}{M_{tot}}, \quad (\text{A4})$$

where M_{12} is the molecular weight of ${}^{12}\text{CH}_4$ (16.03 g/mol). Since ${}^{13}\text{C}$ and ${}^{12}\text{C}$ are the only stable carbon isotopes of CH_4 , 13x and 12x should sum to 1.

Author contributions. A.D. led the data analysis with contributions from P.I.P. and L.F. A.D. led the writing of the paper with contributions from P.I.P., L.F., T.A., X.L., S.M., R.P. and H.M. provided data.

Competing interests. The authors declare that they have no competing interests.

Acknowledgements. A.D. is supported by the University of Edinburgh’s E3 Doctoral Training Partnership, funded by the National Environment Research Council. P.I.P., L.F. and R.P. acknowledge support from the UK National Centre for Earth Observation funded by the National Environment Research Council (NE/R016518/1 and NE/N018079/1) and the Copernicus Climate Change Service (C3S2_312a_Lot2). This work is also supported through a contribution by the National Physical Laboratory, UK to the studentship. We thank NOAA ESRL and CU-INSTAAR for providing CH_4 and $\delta^{13}\text{C}$ data. We thank the Japanese National Institute for Environmental Studies and the Ministry of



Environment for the GOSAT data and their continuous support as part of the Joint Research Agreements at the Universities of Edinburgh and Leicester. We also thank the GEOS-Chem community, particularly the team at Harvard who help maintain the GEOS-Chem model, and the NASA Global Modeling and Assimilation Office (GMAO) who provide the MERRA-2 data product.



375 References

- Bey, I., Jacob, D. J., Yantosca, R. M., Logan, J. A., Field, B. D., Fiore, A. M., Li, Q., Liu, H. Y., Mickley, L. J., and Schultz, M. G.: Global modeling of tropospheric chemistry with assimilated meteorology: Model description and evaluation, *Journal of Geophysical Research Atmospheres*, 106, 23 073–23 095, <https://doi.org/10.1029/2001JD000807>, 2001.
- Bloom, A. A., Bowman, K. W., Lee, M., Turner, A. J., Schroeder, R., Worden, J. R., Weidner, R., Mcdonald, K. C., and Jacob, D. J.: A global
380 wetland methane emissions and uncertainty dataset for atmospheric chemical transport models (WetCHARTs version 1.0), *Geosci. Model Dev*, 10, 2141–2156, <https://doi.org/10.5194/gmd-10-2141-2017>, 2017.
- Burkholder, J. B., Sander, S. P., Abbatt, J., Barker, J. R., Cappa, C., Crouse, J. D., Dibble, T. S. and Huie, R. E., Kolb, C. E., Kurylo, M. J., Orkin, V. L., Percival, C. J., Wilmouth, D. M., and Wine, P. H.: *Chemical Kinetics and Photochemical Data for Use in Atmospheric Studies*, Evaluation No. 19, Tech. rep., JPL Publication 19-5, Jet Propulsion Laboratory, Pasadena, 2019.
- 385 Dlugokencky, E., Crotwell, A., Mund, J., and Thoning, K.: Atmospheric Methane Dry Air Mole Fractions from the NOAA GML Carbon Cycle Cooperative Global Air Sampling Network, 1983–2019, Version: 2020-07, <https://doi.org/https://doi.org/10.15138/VNCZ-M766>, 2020.
- Dlugokencky, E. J., Myers, R. C., Lang, P. M., Masarie, K. A., Crotwell, A. M., Thoning, K. W., Hall, B. D., Elkins, J. W., and Steele, L. P.: Conversion of NOAA atmospheric dry air CH₄ mole fractions to a gravimetrically prepared standard scale, *Journal of Geophysical
390 Research: Atmospheres*, 110, <https://doi.org/10.1029/2005JD006035>, 2005.
- Dlugokencky, E., Steele, L., Lang, P., and Masarie, K.: The growth rate and distribution of atmospheric methane, *Journal of Geophysical Research: Atmospheres*, 99, 17 021–17 043, <https://doi.org/https://doi.org/10.1029/94JD01245>, 1994.
- Douglas, P. M., Stolper, D. A., Eiler, J. M., Sessions, A. L., Lawson, M., Shuai, Y., Bishop, A., Podlaha, O. G., Ferreira, A. A., Santos Neto, E. V., Niemann, M., Steen, A. S., Huang, L., Chimiak, L., Valentine, D. L., Fiebig, J., Luhmann, A. J., Seyfried, W. E., Etiopie, G., Schoell,
395 M., Inskip, W. P., Moran, J. J., and Kitchen, N.: Methane clumped isotopes: Progress and potential for a new isotopic tracer, *Organic Geochemistry*, 113, 262–282, <https://doi.org/10.1016/j.orggeochem.2017.07.016>, 2017.
- Duncan, B. N., Strahan, S. E., Yoshida, Y., Steenrod, S. D., and Livesey, N.: Model study of the cross-tropopause transport of biomass burning pollution, *Atmospheric Chemistry and Physics*, 7, 3713–3736, <https://doi.org/10.5194/acp-7-3713-2007>, 2007.
- Feilberg, K. L., Griffith, D. W. T., Johnson, M. S., and Nielsen, C. J.: The ¹³C and D kinetic isotope effects in the reaction of CH₄ with Cl,
400 *International Journal of Chemical Kinetics*, 37, 110–118, <https://doi.org/https://doi.org/10.1002/kin.20058>, 2005.
- Feng, L., Palmer, P. I., Bösch, H., Parker, R. J., Webb, A. J., Correia, C. S. C., Deutscher, N. M., Domingues, L. G., Feist, D. G., Gatti, L. V., Gloor, E., Hase, F., Kivi, R., Liu, Y., Miller, J. B., Morino, I., Sussmann, R., Strong, K., Uchino, O., Wang, J., and Zahn, A.: Consistent regional fluxes of CH₄ and CO₂ inferred from GOSAT proxy XCH₄ : XCO₂ retrievals, 2010–2014, *Atmospheric Chemistry and Physics*, 17, 4781–4797, <https://doi.org/10.5194/acp-17-4781-2017>, 2017.
- 405 Feng, L., Palmer, P. I., Parker, R. J., Lunt, M. F., and Boesch, H.: Methane emissions responsible for record-breaking atmospheric methane growth rates in 2020 and 2021, *Atmospheric Chemistry and Physics Discussions*, 2022, 1–23, <https://doi.org/10.5194/acp-2022-425>, 2022a.
- Feng, L., Palmer, P. I., Zhu, S., Parker, R. J., and Liu, Y.: Tropical methane emissions explain large fraction of recent changes in global atmospheric methane growth rate, *Nature Communications*, 13, 1378, <https://doi.org/10.1038/s41467-022-28989-z>, 2022b.



- 410 Fraser, A., Palmer, P. I., Feng, L., Bösch, H., Parker, R., Dlugokencky, E. J., Krummel, P. B., and Langenfelds, R. L.: Estimating regional fluxes of CO₂ and CH₄ using space-borne observations of XCH₂: XCO₂, *Atmospheric Chemistry and Physics*, 14, 12 883–12 895, <https://doi.org/10.5194/acp-14-12883-2014>, 2014.
- Fujita, R., Morimoto, S., Maksyutov, S., Kim, H.-S., Arshinov, M., Brailsford, G., Aoki, S., and Nakazawa, T.: Global and Regional CH₄ Emissions for 1995–2013 Derived From Atmospheric CH₄, $\delta^{13}\text{C-CH}_4$, and $\delta\text{D-CH}_4$ Observations and a Chemical Transport
415 Model, *Journal of Geophysical Research: Atmospheres*, 125, e2020JD032 903, <https://doi.org/https://doi.org/10.1029/2020JD032903>, e2020JD032903 2020JD032903, 2020.
- Fung, I., John, J., Lerner, J., Matthews, E., Prather, M., Steele, L. P., and Fraser, P. J.: <Three-dimensional model synthesis of the global methane cycle-Fung 1991.pdf>, *JOURNAL OF GEOPHYSICAL RESEARCH*, 96, 33–46, https://pubs.giss.nasa.gov/docs/1991/1991_{_}Fung_{_}fu08000d.pdf, 1991.
- 420 Ganesan, A. L., Stell, A. C., Gedney, N., Comyn-Platt, E., Hayman, G., Rigby, M., Poulter, B., and Hornibrook, E. R. C.: Spatially Resolved Isotopic Source Signatures of Wetland Methane Emissions, *Geophysical Research Letters*, 45, 3737–3745, <https://doi.org/10.1002/2018GL077536>, 2018.
- Gelaro, R., McCarty, W., Suárez, M. J., Todling, R., Molod, A., Takacs, L., Randles, C. A., Darmenov, A., Bosilovich, M. G., Reichle, R., Wargan, K., Coy, L., Cullather, R., Draper, C., Akella, S., Buchard, V., Conaty, A., da Silva, A. M., Gu, W., Kim, G. K., Koster, R.,
425 Lucchesi, R., Merkova, D., Nielsen, J. E., Partyka, G., Pawson, S., Putman, W., Rienecker, M., Schubert, S. D., Sienkiewicz, M., and Zhao, B.: The modern-era retrospective analysis for research and applications, version 2 (MERRA-2), *Journal of Climate*, 30, 5419–5454, <https://doi.org/10.1175/JCLI-D-16-0758.1>, 2017.
- Gurney, K. R., Law, R. M., Denning, A. S., Rayner, P. J., Baker, D., Bousquet, P., Bruhwiler, L., Chen, Y.-H., Ciais, P., Fan, S., Fung, I. Y., Gloor, M., Heimann, M., Higuchi, K., John, J., Maki, T., Maksyutov, S., Masarie, K., Peylin, P., Prather, M., Pak, B. C., Randerson, J.,
430 Sarmiento, J., Taguchi, S., Takahashi, T., and Yuen, C.-W.: Towards robust regional estimates of CO₂ sources and sinks using atmospheric transport models, *Nature*, 415, 626–630, <https://doi.org/10.1038/415626a>, 2002.
- Kirschke, S., Bousquet, P., Ciais, P., Saunoy, M., Canadell, J. G., Dlugokencky, E. J., Bergamaschi, P., Bergmann, D., Blake, D. R., Bruhwiler, L., Cameron-Smith, P., Castaldi, S., Chevallier, F., Feng, L., Fraser, A., Heimann, M., Hodson, E. L., Houweling, S., Josse, B., Fraser, P. J., Krummel, P. B., Lamarque, J. F., Langenfelds, R. L., Le Quééré, C., Naik, V., O’doherly, S., Palmer, P. I., Pison, I., Plummer, D., Poulter, B., Prinn, R. G., Rigby, M., Ringeval, B., Santini, M., Schmidt, M., Shindell, D. T., Simpson, I. J., Spahni, R., Steele, L. P., Strode, S. A., Sudo, K., Szopa, S., Van Der Werf, G. R., Voulgarakis, A., Van Weele, M., Weiss, R. F., Williams, J. E., and Zeng, G.: Three decades of global methane sources and sinks, <https://doi.org/10.1038/ngeo1955>, 2013.
- Lan, X., Basu, S., Schwietzke, S., Bruhwiler, L. M. P., Dlugokencky, E. J., Michel, S. E., Sherwood, O. A., Tans, P. P., Thoning, K., Etiope, G., Zhuang, Q., Liu, L., Oh, Y., Miller, J. B., Pétron, G., Vaughn, B. H., and Crippa, M.: Improved
440 Constraints on Global Methane Emissions and Sinks Using $\delta^{13}\text{C-CH}_4$, *Global Biogeochemical Cycles*, 35, e2021GB007 000, <https://doi.org/https://doi.org/10.1029/2021GB007000>, e2021GB007000 2021GB007000, 2021.
- Laughner, J. L., Neu, J. L., Schimel, D., Wennberg, P. O., Barsanti, K., Bowman, K. W., Chatterjee, A., Croes, B. E., Fitzmaurice, H. L., Henze, D. K., Kim, J., Kort, E. A., Liu, Z., Miyazaki, K., Turner, A. J., Anenberg, S., Avise, J., Cao, H., Crisp, D., de Gouw, J., Eldering, A., Fyfe, J. C., Goldberg, D. L., Gurney, K. R., Hasheminassab, S., Hopkins, F., Ivey, C. E., Jones, D. B. A., Liu, J., Lovenduski, N. S.,
445 Martin, R. V., McKinley, G. A., Ott, L., Poulter, B., Ru, M., Sander, S. P., Swart, N., Yung, Y. L., and Zeng, Z.-C.: Societal shifts due to COVID-19 reveal large-scale complexities and feedbacks between atmospheric chemistry and climate change, *Proceedings of the National Academy of Sciences*, 118, <https://doi.org/10.1073/pnas.2109481118>, 2021.



- Lunt, M. F., Palmer, P. I., Feng, L., Taylor, C. M., Boesch, H., and Parker, R. J.: An increase in methane emissions from tropical Africa between 2010 and 2016 inferred from satellite data, *Atmospheric Chemistry and Physics*, 19, 14 721–14 740, <https://doi.org/10.5194/acp-19-14721-2019>, 2019.
- Lunt, M. F., Palmer, P. I., Lorente, A., Borsdorff, T., Landgraf, J., Parker, R. J., and Boesch, H.: Rain-fed pulses of methane from East Africa during 2018–2019 contributed to atmospheric growth rate, *Environmental Research Letters*, 16, 024 021, <https://doi.org/10.1088/1748-9326/abd8fa>, 2021.
- McNorton, J., Chipperfield, M. P., Gloor, M., Wilson, C., Feng, W., Hayman, G. D., Rigby, M., Krummel, P. B., O’Doherty, S., Prinn, R. G., Weiss, R. F., Young, D., Dlugokencky, E., and Montzka, S. A.: Role of OH variability in the stalling of the global atmospheric CH₄ growth rate from 1999 to 2006, *Atmospheric Chemistry and Physics*, 16, 7943–7956, <https://doi.org/10.5194/acp-16-7943-2016>, 2016.
- McNorton, J., Wilson, C., Gloor, M., Parker, R., Boesch, H., Feng, W., and Chipperfield, M.: Attribution of recent increases in atmospheric methane through 3-D inverse modelling, *Atmos. Chem. Phys.*, 18, 1–34, <https://doi.org/10.5194/acp-2018-474>, 2018.
- Miller, J. B.: Development of analytical methods and measurements of ¹³C/¹²C in atmospheric CH₄ from the NOAA Climate Monitoring and Diagnostics Laboratory Global Air Sampling Network, *Journal of Geophysical Research*, 107, 4178, <https://doi.org/10.1029/2001JD000630>, 2002.
- Miyazaki, K., Bowman, K., Sekiya, T., Takigawa, M., Neu, J. L., Sudo, K., Osterman, G., and Eskes, H.: Global tropospheric ozone responses to reduced NO_x emissions linked to the COVID-19 worldwide lockdowns, *Science Advances*, 7, eabf7460, <https://doi.org/10.1126/sciadv.abf7460>, 2021.
- Nisbet, E. G., Dlugokencky, E. J., Manning, M. R., Lowry, D., Fisher, R. E., France, J. L., Michel, S. E., Miller, J. B., White, J. W., Vaughn, B., Bousquet, P., Pyle, J. A., Warwick, N. J., Cain, M., Brownlow, R., Zazzeri, G., Lanoisellé, M., Manning, A. C., Gloor, E., Worthy, D. E., Brunke, E. G., Labuschagne, C., Wolff, E. W., and Ganesan, A. L.: Rising atmospheric methane: 2007–2014 growth and isotopic shift, *Global Biogeochemical Cycles*, 30, 1356–1370, <https://doi.org/10.1002/2016GB005406>, 2016.
- Nisbet, E. G., Manning, M. R., Dlugokencky, E. J., Fisher, R. E., Lowry, D., Michel, S. E., Myhre, C. L., Platt, S. M., Allen, G., Bousquet, P., Brownlow, R., Cain, M., France, J. L., Hermansen, O., Hossaini, R., Jones, A. E., Levin, I., Manning, A. C., Myhre, G., Pyle, J. A., Vaughn, B. H., Warwick, N. J., and White, J. W. C.: Very Strong Atmospheric Methane Growth in the 4 Years 2014–2017: Implications for the Paris Agreement, *Global Biogeochemical Cycles*, 33, 318–342, <https://doi.org/https://doi.org/10.1029/2018GB006009>, 2019.
- Palmer, P. I., Feng, L., Lunt, M. F., Parker, R. J., Bösch, H., Lan, X., Lorente, A., and Borsdorff, T.: The added value of satellite observations of methane for understanding the contemporary methane budget, *Philosophical Transactions of the Royal Society A: Mathematical, Physical and Engineering Sciences*, 379, 20210 106, <https://doi.org/10.1098/rsta.2021.0106>, 2021.
- Pandey, S., Houweling, S., Lorente, A., Borsdorff, T., Tsvilidou, M., Bloom, A. A., Poulter, B., Zhang, Z., and Aben, I.: Using satellite data to identify the methane emission controls of South Sudan’s wetlands, *Biogeosciences*, 18, 557–572, <https://doi.org/10.5194/bg-18-557-2021>, 2021.
- Parker, R., Boesch, H., Cogan, A., Fraser, A., Feng, L., Palmer, P. I., Messerschmidt, J., Deutscher, N., Griffith, D. W. T., Notholt, J., Wennberg, P. O., and Wunch, D.: Methane observations from the Greenhouse Gases Observing SATellite: Comparison to ground-based TCCON data and model calculations, *Geophysical Research Letters*, 38, <https://doi.org/https://doi.org/10.1029/2011GL047871>, 2011.
- Parker, R. J., Boesch, H., Byckling, K., Webb, A. J., Palmer, P. I., Feng, L., Bergamaschi, P., Chevallier, F., Notholt, J., Deutscher, N., Warneke, T., Hase, F., Sussmann, R., Kawakami, S., Kivi, R., Griffith, D. W. T., and Velazco, V.: Assessing 5 years of GOSAT Proxy XCH₄ data and associated uncertainties, *Atmospheric Measurement Techniques*, 8, 4785–4801, <https://doi.org/10.5194/amt-8-4785-2015>, 2015.



- Parker, R. J., Webb, A., Boesch, H., Somkuti, P., Barrio Guillo, R., Di Noia, A., Kalaitzi, N., Anand, J. S., Bergamaschi, P., Chevallier, F., Palmer, P. I., Feng, L., Deutscher, N. M., Feist, D. G., Griffith, D. W. T., Hase, F., Kivi, R., Morino, I., Notholt, J., Oh, Y.-S., Ohyama, H., Petri, C., Pollard, D. F., Roehl, C., Sha, M. K., Shiomu, K., Strong, K., Sussmann, R., Té, Y., Velazco, V. A., Warneke, T., Wennberg, P. O., and Wunch, D.: A decade of GOSAT Proxy satellite CH₄ observations, *Earth System Science Data*, 12, 3383–3412, 490 <https://doi.org/10.5194/essd-12-3383-2020>, 2020.
- Randerson, J., Van Der Werf, G., Giglio, L., Collatz, G., and Kasibhatla, P.: Global Fire Emissions Database, Version 4.1 (GFEDv4), <https://doi.org/10.3334/ORNLDAAC/1293>, 2017.
- Rice, A. L., Butenhoff, C. L., Teama, D. G., Röger, F. H., Khalil, M. A. K., and Rasmussen, R. A.: Atmospheric methane isotopic record favors fossil sources flat in 1980s and 1990s with recent increase, *Proceedings of the National Academy of Sciences*, 113, 10 791–10 796, 495 <https://doi.org/10.1073/pnas.1522923113>, 2016.
- Rigby, M., Montzka, S. A., Prinn, R. G., White, J. W. C., Young, D., O’Doherty, S., Lunt, M. F., Ganesan, A. L., Manning, A. J., Simmonds, P. G., Salameh, P. K., Harth, C. M., Mühle, J., Weiss, R. F., Fraser, P. J., Steele, L. P., Krummel, P. B., McCulloch, A., and Park, S.: Role of atmospheric oxidation in recent methane growth, *Proceedings of the National Academy of Sciences*, 114, 5373–5377, <https://doi.org/10.1073/pnas.1616426114>, 2017.
- 500 Sasakawa, M., Shimoyama, K., Machida, T., Tsuda, N., Suto, H., Arshinov, M., Davydov, D., Fofonov, A., Krasnov, O., Saeki, T., Koyama, Y., and Maksyutov, S.: Continuous measurements of methane from a tower network over Siberia, *Tellus B*, 62, 403–416, <https://doi.org/https://doi.org/10.1111/j.1600-0889.2010.00494.x>, 2010.
- Saunois, M., Bousquet, P., Poulter, B., Pregon, A., Ciais, P., Canadell, J. G., Dlugokencky, E. J., Etiope, G., Bastviken, D., Houweling, S., Janssens-Maenhout, G., Tubiello, F. N., Castaldi, S., Jackson, R. B., Alexe, M., Arora, V. K., Beerling, D. J., Bergamaschi, P., Blake, D. R., 505 Brailsford, G., Brovkin, V., Bruhwiler, L., Crevoisier, C., Crill, P., Covey, K., Curry, C., Frankenberg, C., Gedney, N., Höglund-Isaksson, L., Ishizawa, M., Ito, A., Joos, F., Kim, H.-S., Kleinen, T., Krummel, P., Lamarque, J.-F., Langenfelds, R., Locatelli, R., Machida, T., Maksyutov, S., Mcdonald, K. C., Marshall, J., Melton, J. R., Morino, I., Naik, V., O’Doherty, S., Parmentier, F.-J. W., Patra, P. K., Peng, C., Peng, S., Peters, G. P., Pison, I., Prigent, C., Prinn, R., Ramonet, M., Riley, W. J., Saito, M., Santini, M., Schroeder, R., Simpson, I. J., Spahni, R., Steele, P., Takizawa, A., Thornton, B. F., Tian, H., Tohjima, Y., Viovy, N., Voulgarakis, A., Van Weele, M., Van Der Werf, 510 G. R., Weiss, R., Wiedinmyer, C., Wilton, D. J., Wiltshire, A., Worthy, D., Wunch, D., Xu, X., Yoshida, Y., Zhang, B., Zhang, Z., and Zhu, Q.: The global methane budget 2000–2012, *Earth Syst. Sci. Data*, 8, 697–751, <https://doi.org/10.5194/essd-8-697-2016>, 2016.
- Schaefer, H., Schaefer, H., Fletcher, S. E. M., Veidt, C., Lassey, K. R., Brailsford, G. W., Bromley, M., Dlugokencky, E. J., Michel, S. E., Miller, J. B., Levin, I., Lowe, D. C., Martin, J., Vaughn, B. H., and White, J. W. C.: A 21st century shift from fossil-fuel to biogenic methane emissions indicated by 13CH₄, *Science*, 2705, 1–10, 2016.
- 515 Schultdt, K. N., Aalto, T., Andrews, A., Aoki, S., Arduini, J., Baier, B., Bergamaschi, P., Biermann, T., Biraud, S. C., Boenisch, H., Brailsford, G., Chen, H., Colomb, A., Conil, S., Cristofanelli, P., Cuevas, E., Daube, B., Davis, K., Mazière, M. D., Delmotte, M., Desai, A., DiGangi, J. P., Dlugokencky, E., Elkins, J. W., Emmenegger, L., Fischer, M. L., Gatti, L. V., Gehrlein, T., Gerbig, C., Gloor, E., Goto, D., Haszpra, L., Hatakka, J., Heimann, M., Heliasz, M., Hermanssen, O., Hintsä, E., Holst, J., Ivakhov, V., Jaffe, D., Joubert, W., Kang, H.-Y., Karion, A., Kazan, V., Keronen, P., Ko, M.-Y., Kominkova, K., Kort, E., Kozlova, E., Krummel, P., Kubistin, D., Labuschagne, C., Langenfelds, R., Laurent, O., Laurila, T., Lauvaux, T., Lee, J., Lee, H., Lee, C.-H., Lehner, I., Leppert, R., Leuenberger, M., Lindauer, M., Loh, Z., Lopez, M., Machida, T., Mammarella, I., Manca, G., Marek, M. V., Martin, M. Y., Matsueda, H., McKain, K., Miles, N., Miller, C. E., Miller, J. B., Moore, F., Morimoto, S., Munro, D., Myhre, C. L., Mölder, M., Müller-Williams, J., Nichol, S., Niwa, Y., O’Doherty, S., 520 Obersteiner, F., Piacentino, S., Pichon, J. M., Pittman, J., Plass-Duelmer, C., Ramonet, M., Richardson, S., Rivas, P. P., Saito, K., Santoni,



- 525 G., Sasakawa, M., Scheeren, B., Schuck, T., Schumacher, M., Seifert, T., Sha, M. K., Shepson, P., Sloop, C. D., Smith, P., Steinbacher, M., Stephens, B., Sweeney, C., Timas, H., Torn, M., Trisolino, P., Turnbull, J., Tørseth, K., Viner, B., Vitkova, G., Watson, A., Wofsy, S., Worsley, J., Worthy, D., Zahn, A., and di Sarra, A. G.: Multi-laboratory compilation of atmospheric methane data for the period 1983–2020; obspack_ch4_1_GLOBALVIEWplus_v4.0_2021-10-14, <https://doi.org/http://doi.org/10.25925/20211001>, 2021.
- 530 Sheng, J., Tunnicliffe, R., Ganesan, A. L., Maasackers, J. D., Shen, L., Prinn, R. G., Song, S., Zhang, Y., Scarpelli, T., Bloom, A. A., Rigby, M., Manning, A. J., Parker, R. J., Boesch, H., Lan, X., Zhang, B., Zhuang, M., and Lu, X.: Sustained methane emissions from China after 2012 despite declining coal production and rice-cultivated area, *Environmental Research Letters*, 16, 104018, <https://doi.org/10.1088/1748-9326/ac24d1>, 2021.
- 535 Sherwen, T., Schmidt, J. A., Evans, M. J., Carpenter, L. J., Großmann, K., Eastham, S. D., Jacob, D. J., Dix, B., Koenig, T. K., Sinreich, R., Ortega, I., Volkamer, R., Saiz-Lopez, A., Prados-Roman, C., Mahajan, A. S., and Ordóñez, C.: Global impacts of tropospheric halogens (Cl, Br, I) on oxidants and composition in GEOS-Chem, *Atmospheric Chemistry and Physics*, 16, 12 239–12 271, <https://doi.org/10.5194/acp-16-12239-2016>, 2016.
- Sherwood, O. A., Schwietzke, S., Arling, V. A., and Etiope, G.: Global inventory of gas geochemistry data from fossil fuel, microbial and burning sources, version 2017, *Earth System Science Data*, 9, 639–656, <https://doi.org/10.5194/essd-9-639-2017>, 2017.
- Snover, A. K. and Quay, P. D.: Hydrogen and carbon kinetic isotope effects during soil uptake of atmospheric methane, *Global Biogeochemical Cycles*, 14, 25–39, <https://doi.org/10.1029/1999GB900089>, 2000.
- 540 Source: European Commission, J. R. C. J. E. A. A. P.: Emission Database for Global Atmospheric Research (EDGAR), release version 4.2., <http://edgar.jrc.ec.europa.eu>, 2011.
- Steele, L. P., Fraser, P. J., Rasmussen, R. A., Khalil, M. A. K., Conway, T. J., Crawford, A. J., Gammon, R. H., Masarie, K. A., and Thoning, K. W.: *The Global Distribution of Methane in the Troposphere*, pp. 417–463, Springer Netherlands, 1987.
- 545 Turner, A. J., Frankenberg, C., Wennberg, P. O., and Jacob, D. J.: Ambiguity in the causes for decadal trends in atmospheric methane and hydroxyl, *Proceedings of the National Academy of Sciences*, 114, 5367–5372, <https://doi.org/10.1073/pnas.1616020114>, 2017.
- Turner, A. J., Frankenberg, C., and Kort, E. A.: Interpreting contemporary trends in atmospheric methane, *Proceedings of the National Academy of Sciences*, 116, 201814 297, <https://doi.org/10.1073/pnas.1814297116>, 2019.
- Vaughn, B., Miller, J., Ferretti, D., and White, J.: Stable isotope measurements of atmospheric CO₂ and CH₄, *Handbook of Stable Isotope Analytical Techniques*, vol 1, chap. 14, Elsevier, 2004.
- 550 Wilson, C., Chipperfield, M. P., Gloor, M., Parker, R. J., Boesch, H., McNorton, J., Gatti, L. V., Miller, J. B., Basso, L. S., and Monks, S. A.: Large and increasing methane emissions from eastern Amazonia derived from satellite data, 2010–2018, *Atmospheric Chemistry and Physics*, 21, 10 643–10 669, <https://doi.org/10.5194/acp-21-10643-2021>, 2021.
- Worden, J., Bloom, A., Pandey, S., Jiang, Z., Worden, H., Walker, T., Houweling, S., and Röckmann, T.: Reduced biomass burning emissions reconcile conflicting estimates of the post-2006 atmospheric methane budget, *Nature Communications*, 8, <https://doi.org/10.1038/s41467-017-02246-0>, 2017.
- 555 Yin, Y., Chevallier, F., Ciais, P., Bousquet, P., Saunois, M., Zheng, B., Worden, J., Bloom, A. A., Parker, R. J., Jacob, D. J., Dlugokencky, E. J., and Frankenberg, C.: Accelerating methane growth rate from 2010 to 2017: leading contributions from the tropics and East Asia, *Atmospheric Chemistry and Physics*, 21, 12 631–12 647, <https://doi.org/10.5194/acp-21-12631-2021>, 2021.
- Zazzeri, G., Lowry, D., Fisher, R. E., France, J. L., Lanoisellé, M., Kelly, B. F. J., Necki, J. M., Iverach, C. P., Ginty, E., Zimnoch, M., Jasek, A., and Nisbet, E. G.: Carbon isotopic signature of coal-derived methane emissions to the atmosphere: from coalification to alteration, *Atmospheric Chemistry and Physics*, 16, 13 669–13 680, <https://doi.org/10.5194/acp-16-13669-2016>, 2016.
- 560



- 565 Zhao, Y., Saunio, M., Bousquet, P., Lin, X., Berchet, A., Hegglin, M. I., Canadell, J. G., Jackson, R. B., Hauglustaine, D. A., Szopa, S., Stavert, A. R., Abraham, N. L., Archibald, A. T., Bekki, S., Deushi, M., Jöckel, P., Josse, B., Kinnison, D., Kirner, O., Marécal, V., O'Connor, F. M., Plummer, D. A., Revell, L. E., Rozanov, E., Stenke, A., Strode, S., Tilmes, S., Dlugokencky, E. J., and Zheng, B.: Inter-model comparison of global hydroxyl radical (OH) distributions and their impact on atmospheric methane over the 2000–2016 period, *Atmospheric Chemistry and Physics*, 19, 13 701–13 723, <https://doi.org/10.5194/acp-19-13701-2019>, 2019.
- Zhou, L., Kitzis, D., and Tans, P.: Report of the Fourth WMO Round-Robin Reference Gas Intercomparison, 2002-2007, Tech. rep., World Meteorological Organisation, 2009.

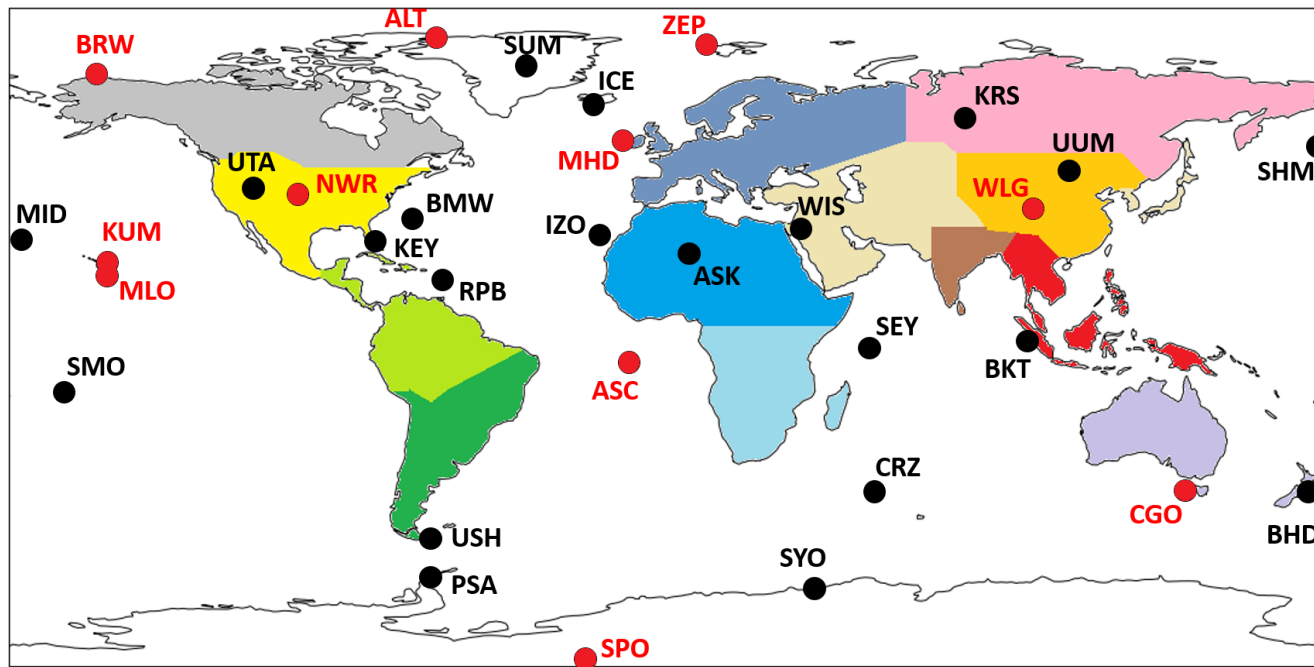


Figure 1. Map showing regions that are optimised in the CH_4 and $\delta^{13}\text{C}$ inversions, in different colours. Black dots and labels show the location of ground-based *in situ* measuring sites that measure CH_4 mole fraction. Red dots and labels indicate both total CH_4 and $\delta^{13}\text{C}$ measuring sites. Regions are named as follows: Grey - North American Boreal; Yellow - North American Temperate; Light Green - South American Tropical; Dark Green - South American Temperate; Purple - Europe; Blue - North Africa; Light Blue - Southern Africa; Pink - Boreal Eurasia; Orange - China; Brown - India; Peach - Temperate Eurasia; Red - Tropical SE Asia; Lilac - Oceania; White - Oceans. Site identifiers are detailed in Table A1.

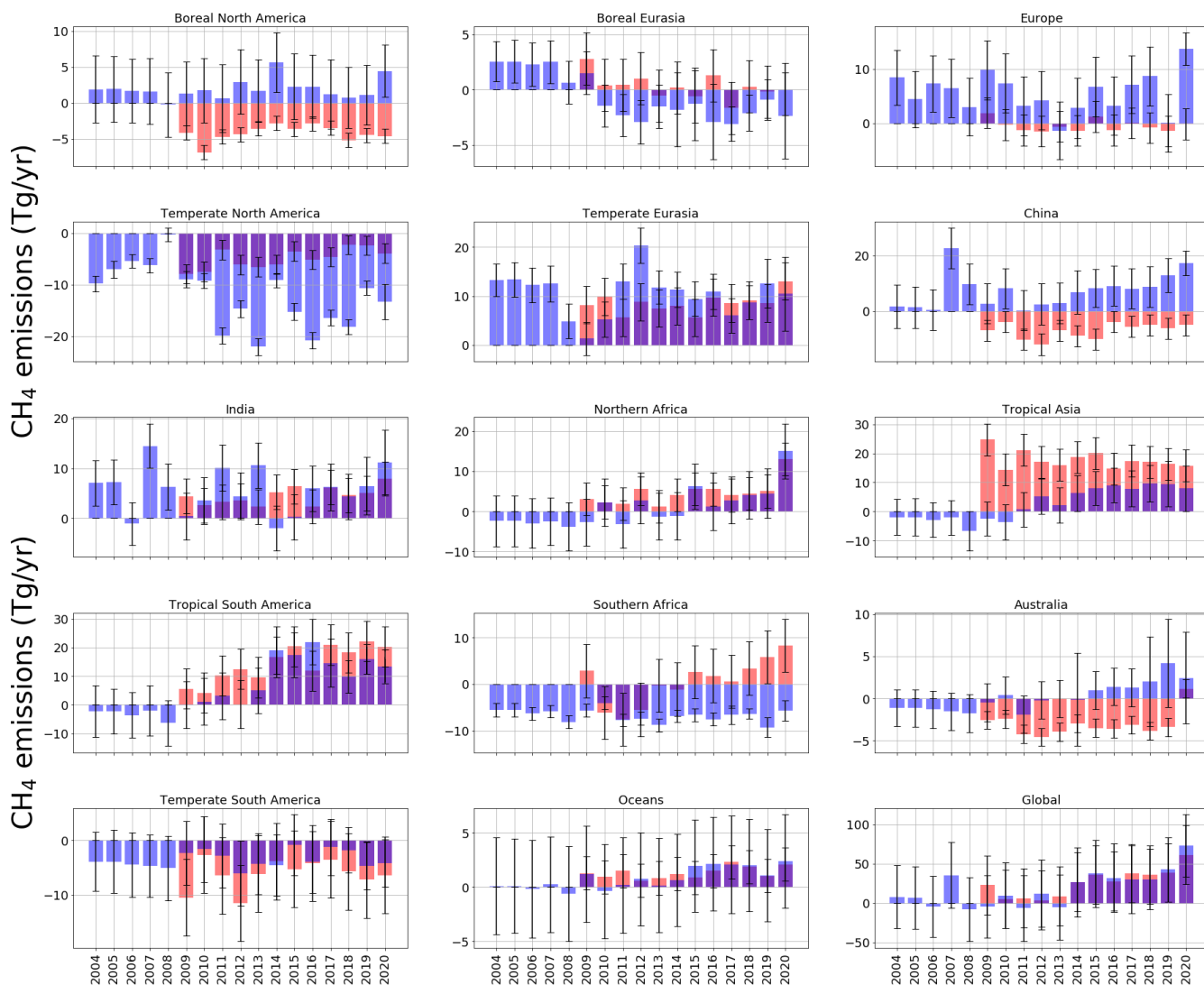


Figure 2. Annual mean CH₄ emissions (Tg/yr) from each of the inversion regions in latitudinal order (geographic coverage indicated by Figure 1), for both ground-based and GOSAT inversion results. The emissions are shown as a residual value, relative to the *a priori* yearly emission for each region. Uncertainties in yearly emissions are indicated, as calculated from inversion calculations, with a *a priori* uncertainty of 50 % for the *in situ* results and 60 % for the GOSAT results. The ground-based *a posteriori* is in blue; the GOSAT *a posteriori* are in red.

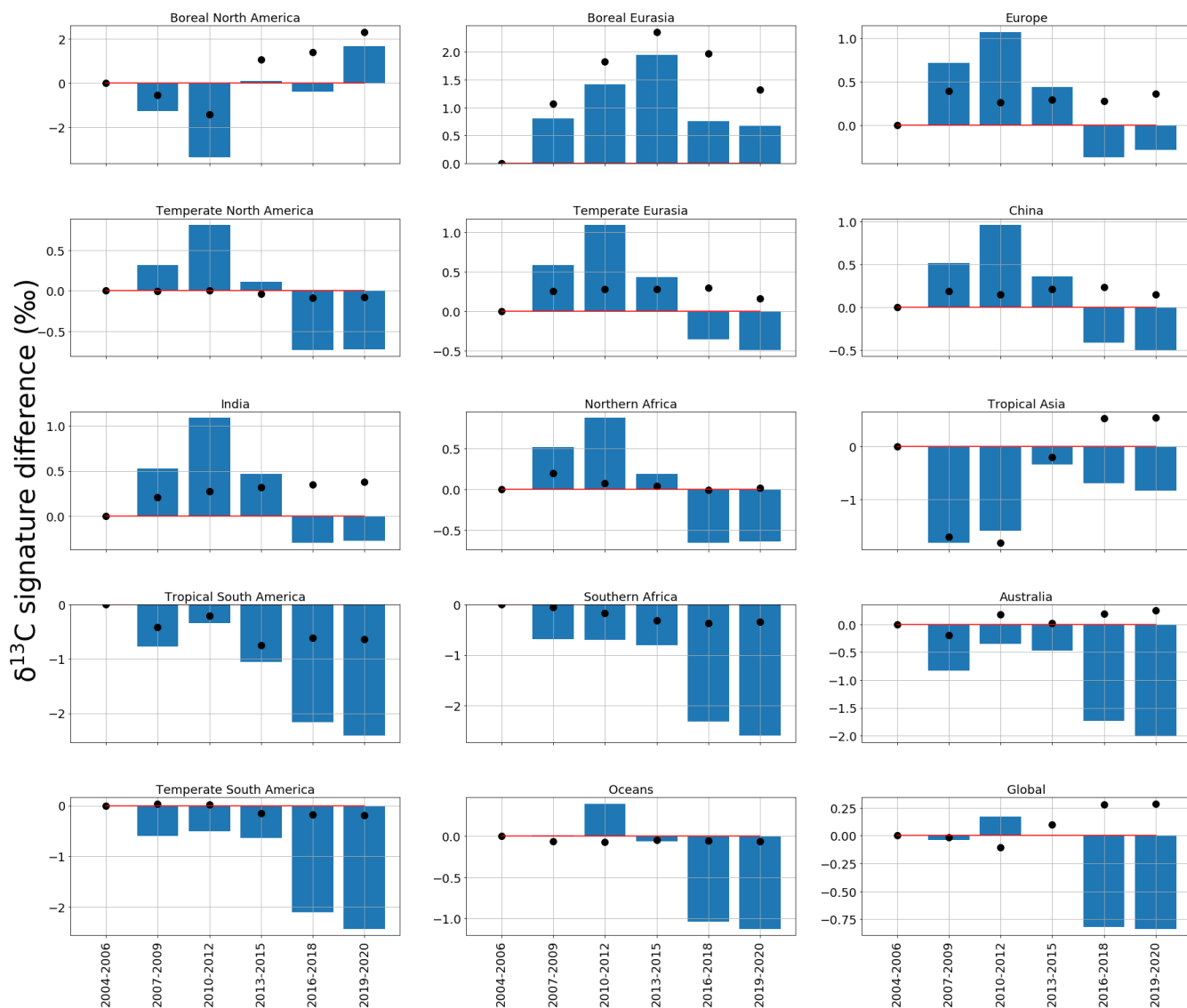


Figure 3. Regional and global *a posteriori* $\delta^{13}\text{C}$ emissions source signatures (‰), in three-yearly groups (2004-06, 2007-09, 2010-12, 2013-15, 2016-18, 2019-20) as a residual from the 2004-06 *a posteriori* regional emissions source signature value. The *a priori* equivalent is represented by black dots. The regions are those solved for in the CH_4 and $\delta^{13}\text{C}$ inversions and are indicated by Figure 1.

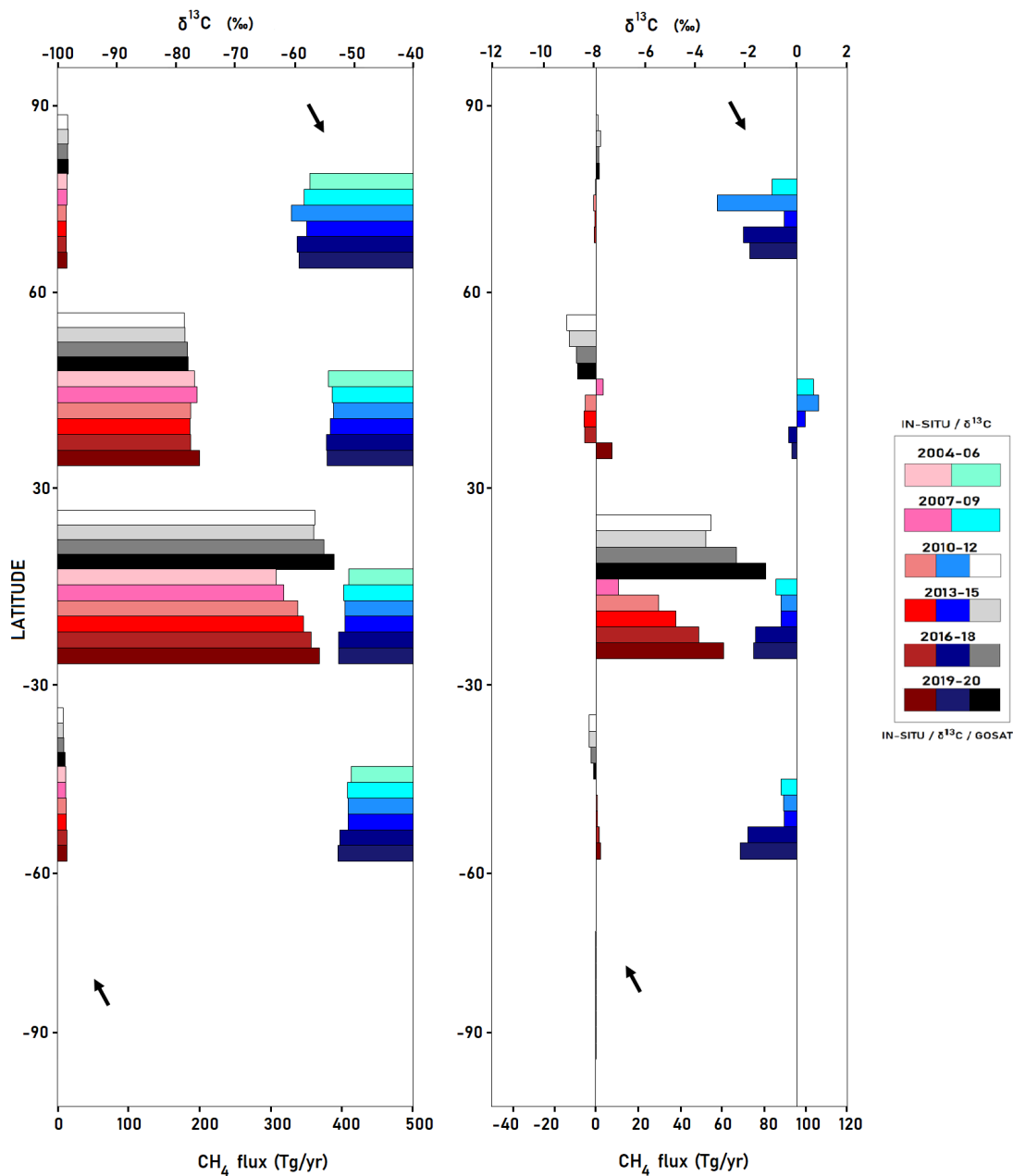


Figure 4. Triennial mean CH_4 emission anomalies (Tg/yr) from 2004 to 2020 for NOAA data (denoted by shades of red) and from 2010 to 2020 for GOSAT data (denoted by shades of grey), and triennial mean $\delta^{13}\text{C}$ emissions source signatures (‰ , denoted by shades of blue) from 2004 to 2020, all grouped every 30° latitude. Anomalies are defined relative to the 2004–2006 mean values.

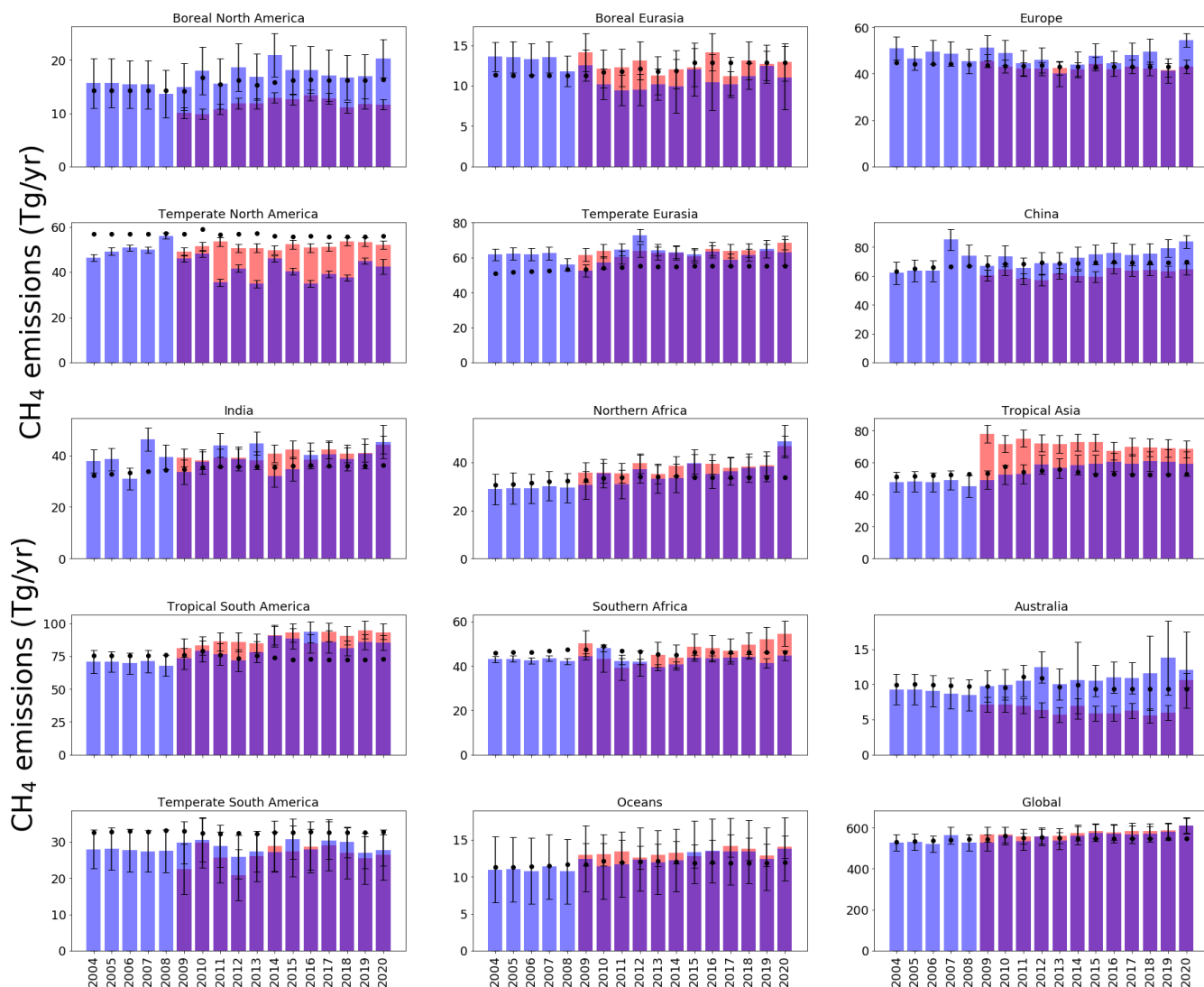


Figure A1. *A posteriori* emissions estimates (Tg/yr) inferred from ground-based *in situ* data (blue) and GOSAT data (red, with record starting in 2010) for the geographical regions shown by Figure 1. *A priori* emissions estimates are denoted by black dots and *a posteriori* uncertainties are denoted by whisker bars.

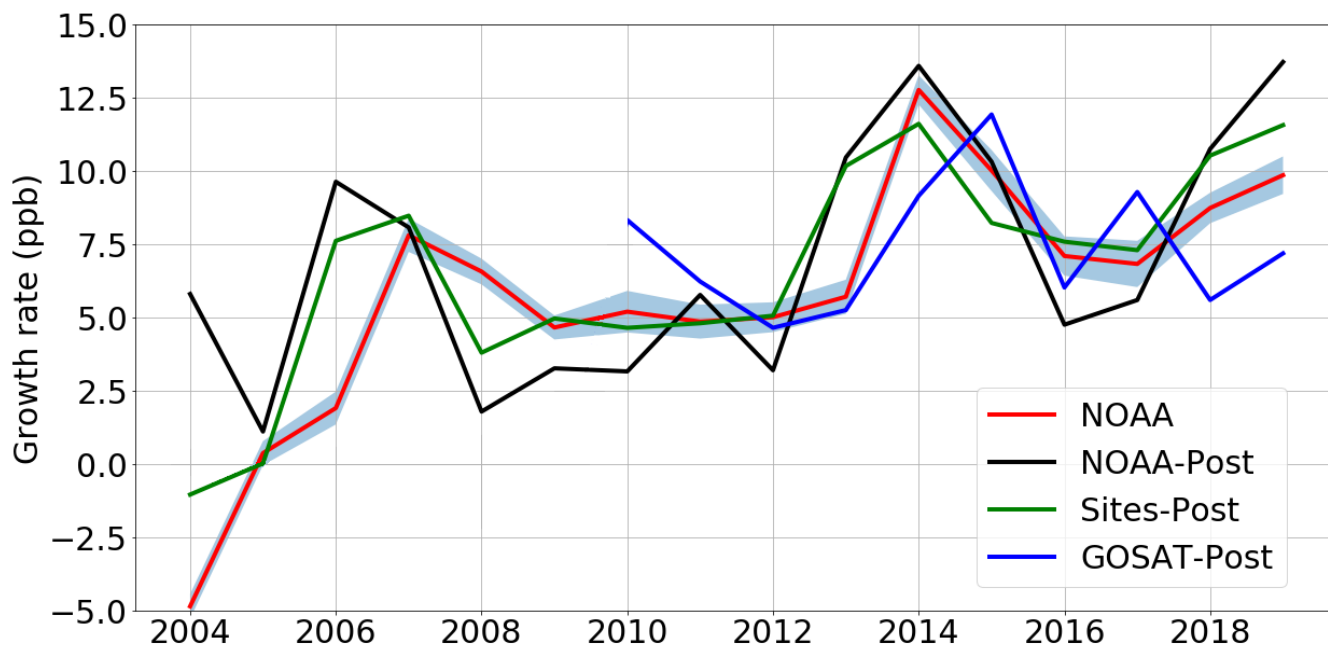


Figure A2. A *posteriori* annual mean atmospheric CH₄ growth rate inferred from *in situ* (black line) and GOSAT data (blue line) compared with the equivalent data as published by NOAA (red line, Dlugokencky et al., 2020). The green line denotes the annual atmospheric growth rate determined using the *in situ* mole fraction data from the sites included in the inversion ('Sites-Post'). To calculate the atmospheric growth rates from model calculations (NOAA-Post and GOSAT-post), we compare the average global CH₄ mole fraction in one year (the mean mole fraction of every grid square in every month of a year), with the mean value from the following year. The calculation is January-January, in order to remove the effects of the seasonal cycle, following the approach by NOAA (Dlugokencky et al., 2020).

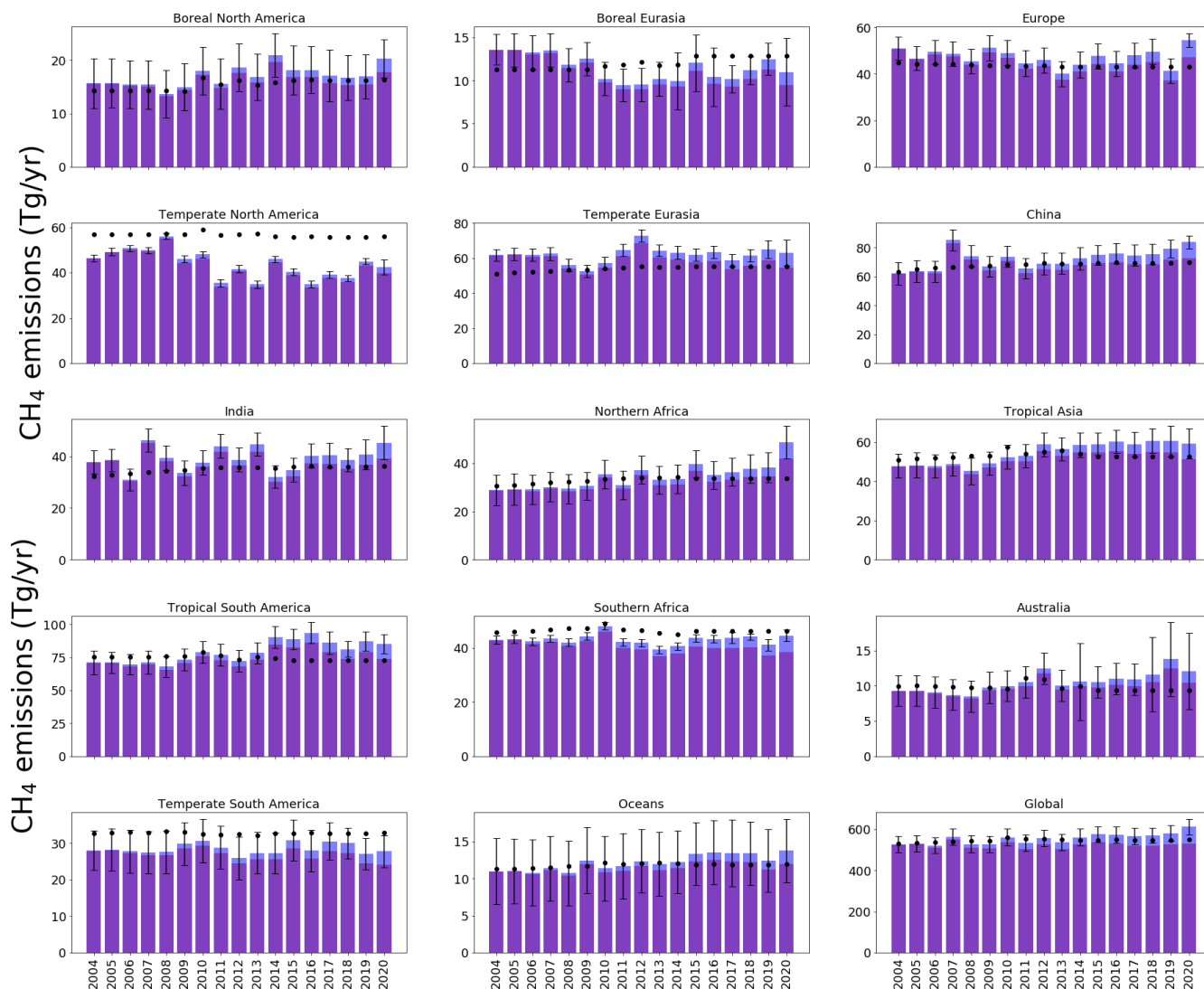


Figure A3. Annual mean CH₄ emissions (Tg/yr) for each region of the inversion (indicated by Figure 1) inferred from the ground-based data (dark blue) and the emissions estimates determined by a reduced OH values (described in the text, shown in red). *A priori* regional emissions estimates are indicated by black dots. Regional uncertainties for the *a posteriori* emissions are indicated.

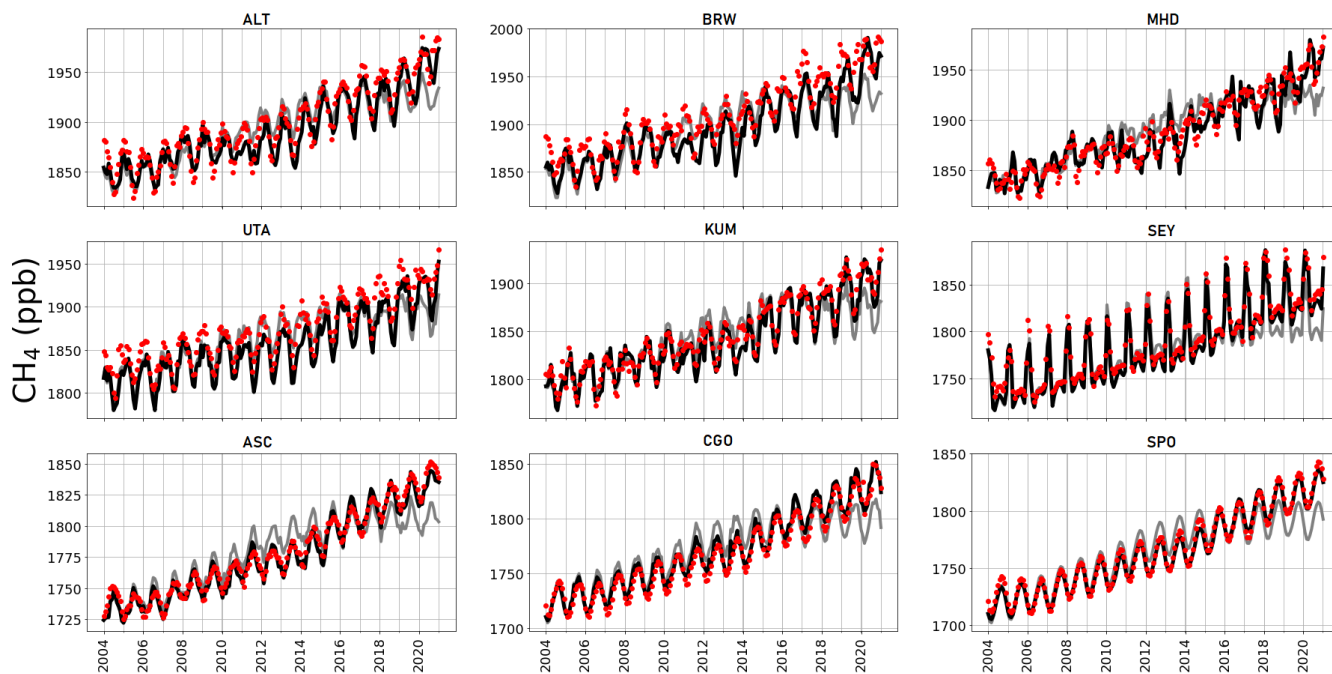


Figure A4. Observed (red dots), and *a priori* (grey), *a posteriori* (black) model atmospheric mole fractions at a series of NOAA sites (subplot titles denote site codes, Table A1), covering a range of latitudes.

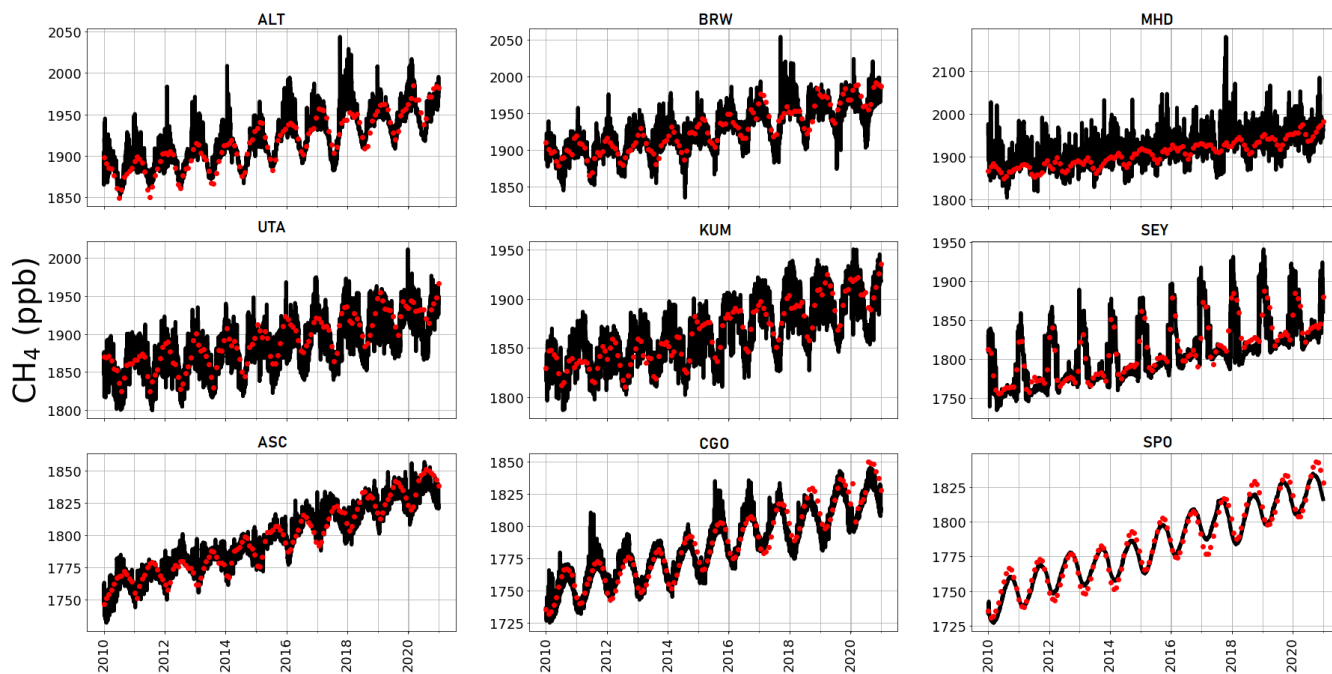


Figure A5. Observed (red dots), and three-hourly surface *a posteriori* CH_4 values inferred from GOSAT data (black) at the location of a number of NOAA sites (Table A1) 2010-2020.

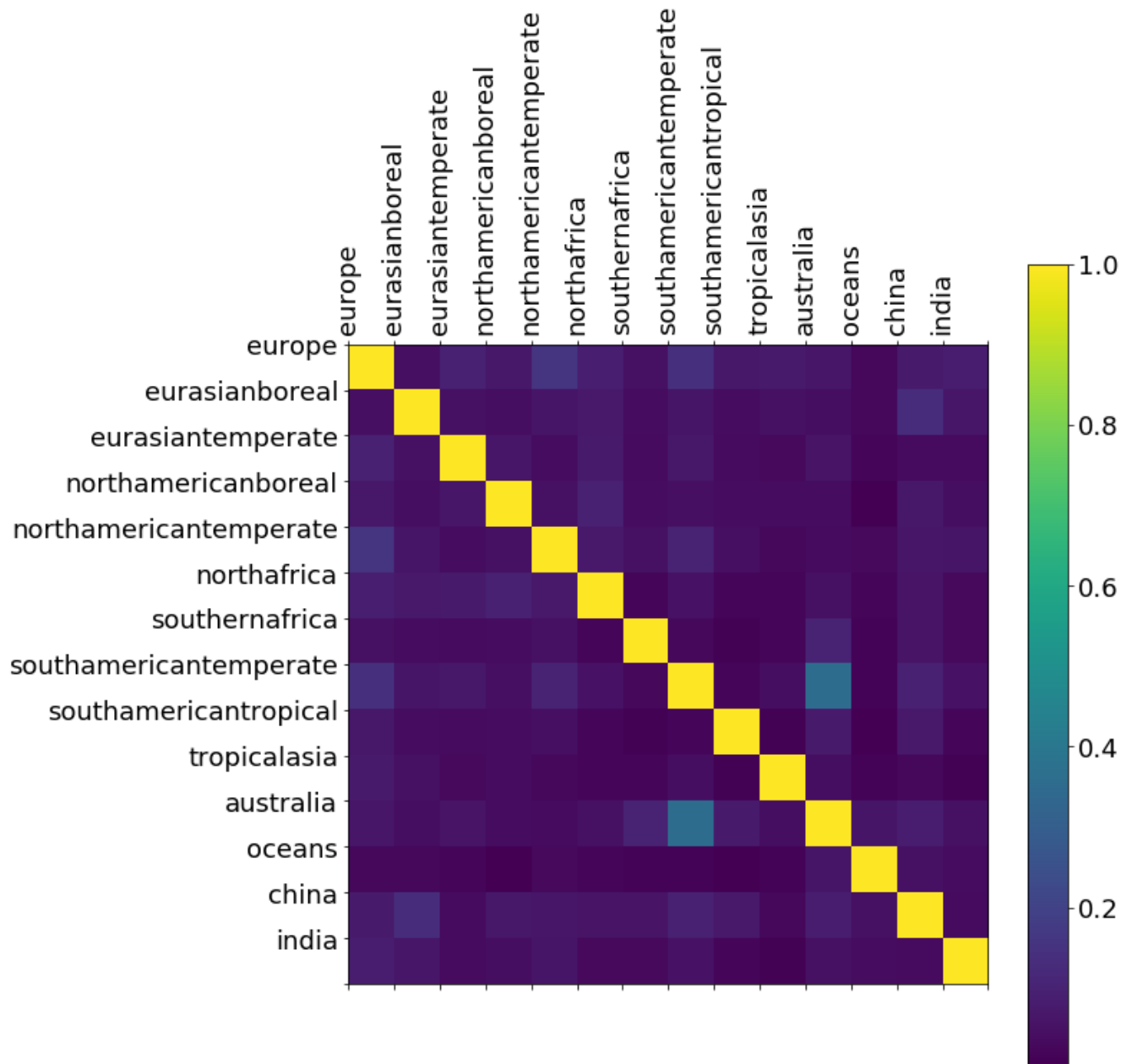


Figure A6. *A posteriori* correlations between CH₄ emissions from geographical regions inferred from NOAA CH₄ mole fraction data. These correlations are determined by normalising the diagonal elements of the *a posteriori* error covariance matrix (Eq. (2)).

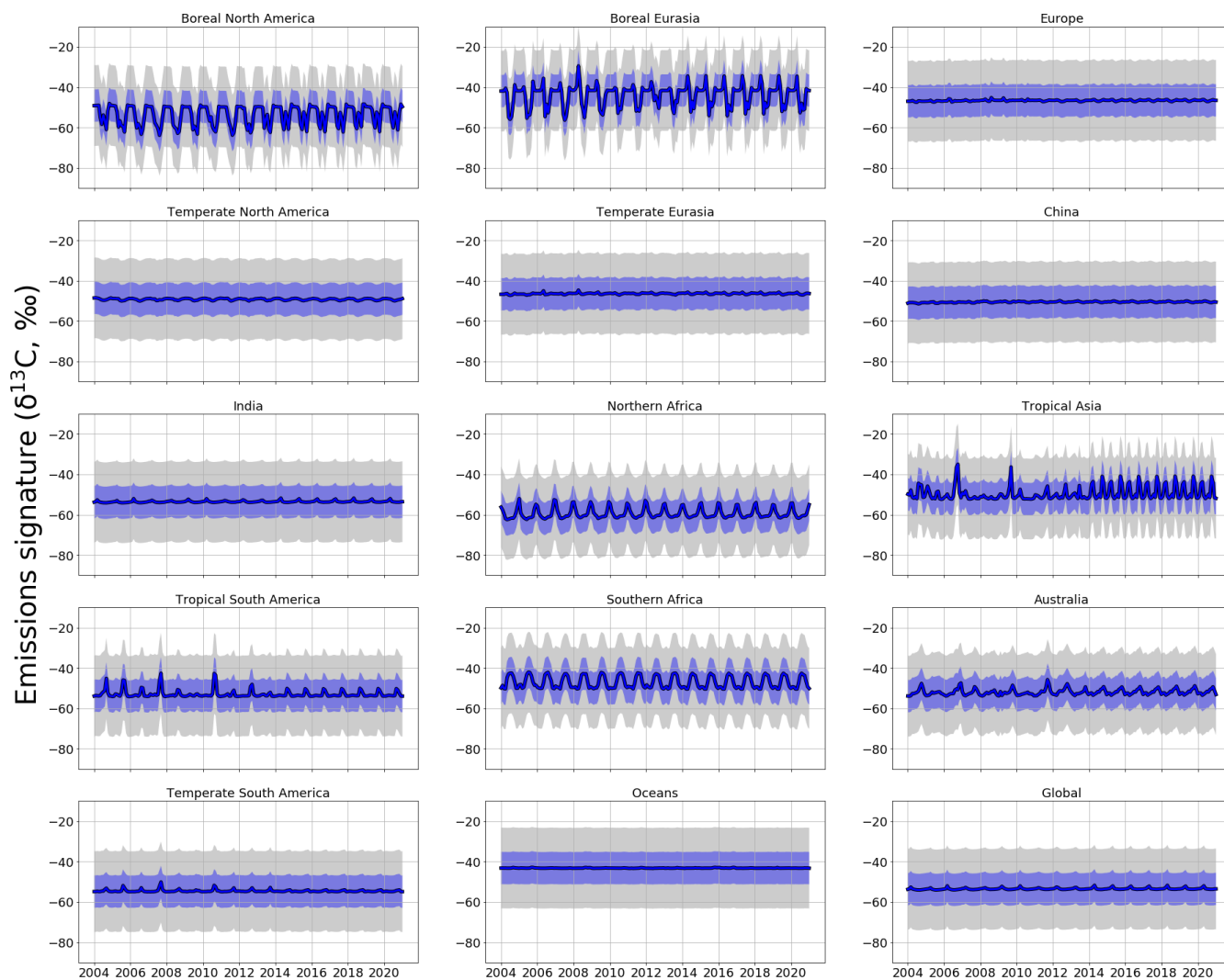


Figure A7. Monthly *a priori* (grey) and *a posteriori* (blue) regional $\delta^{13}\text{C}$ source signatures (‰). Values are produced using ground-based *in situ* $\delta^{13}\text{C}$ data. Uncertainties in source signatures are indicated as shaded envelopes, with *a priori* uncertainties of 15 ‰.

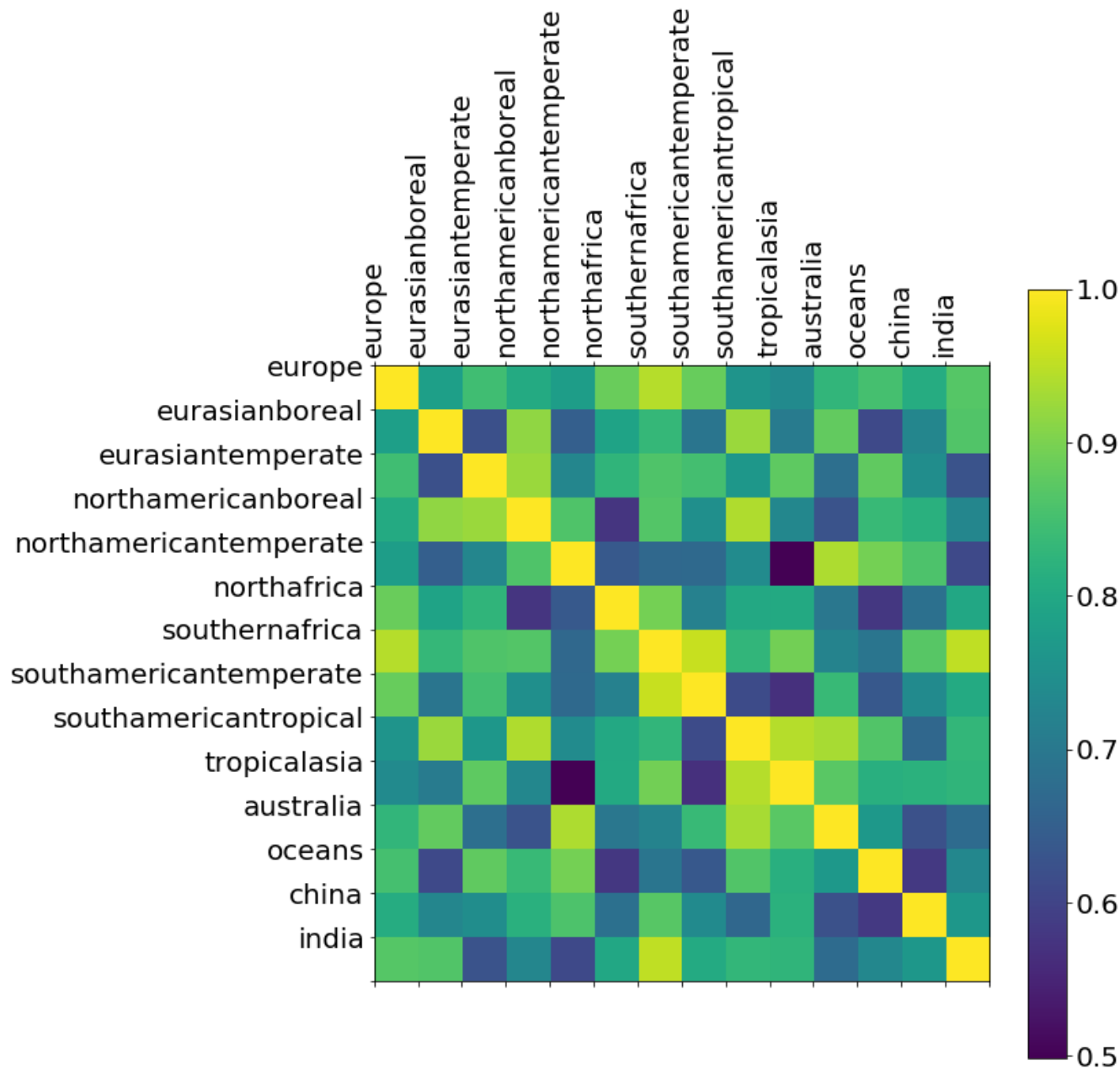


Figure A8. *A posteriori* correlations between $\delta^{13}\text{C}$ source signatures from geographical regions inferred from ground-based $\delta^{13}\text{C}$ data. These correlations are determined by normalising the diagonal elements of the *a posteriori* error covariance matrix (Equation 2).

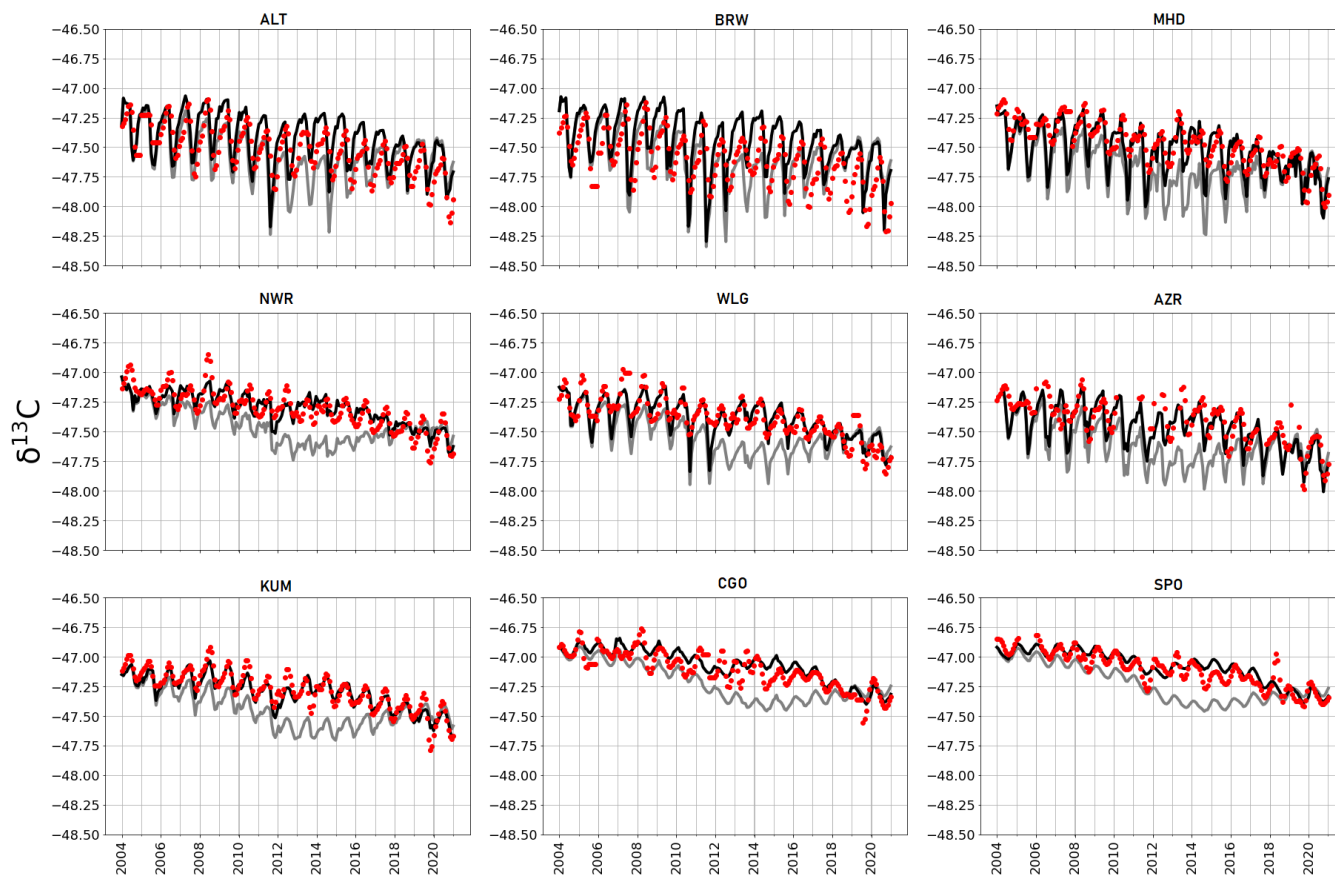


Figure A9. *A priori* (grey) and *a posteriori* (black) monthly estimates of atmospheric $\delta^{13}\text{C}$, simulated at NOAA sites across latitudes (site codes listed in Table A1). Red dots indicate monthly mean $\delta^{13}\text{C}$ data from CU-INSTAAR for the respective sites.



Table 1. Magnitudes of different CH₄ source types and the corresponding conventional isotope ratios (Sherwood et al., 2017). Magnitudes are from bottom-up inventories (Saunio et al., 2016), with uncertainties as max-min values in square brackets.

Source Type	Annual Mean Emission 2003-2012 (Tg/CH ₄)	Isotopic Ratio $\delta^{13}\text{C}$
Gas and Oil	79 [69-88]	-44.0
Coal	41 [26-50]	-49.5
Livestock	106 [97-11]	-65.4
Waste	195 [178-206]	-56.0
Biomass Burning	18 [15-20]	-26.2
Termites	9 [3-15]	-63.4
Wetlands	185 [153-227]	-61.5 (Tropical) -71.5 (Arctic)
Rice	30 [27-35]	-62.2



Table 2. Kinetic Isotope Effects (KIEs) for different isotopologues reacting with the three main sinks of CH₄ (OH, Cl, soil) at 298K. A KIE indicates relative reaction rate compared with ¹²CH₄; the reaction rate constant is applied to the OH and Cl sinks and is dependent upon temperature (T); and the scaling factor is applied to the soil sink at each timestep (handled as a negative emission).

Isotopologue	Sink	KIE	Reaction Rate Constant	Scaling Factor	Literature Source
¹² CH ₄	OH	1	$2.45 \times 10^{-12} \times e^{\frac{-1775}{T}}$	n/a	Burkholder et al., 2019
¹² CH ₄	Cl	1	$9.600 \times 10^{-12} \times e^{\frac{-1360}{T}}$	n/a	Kirschke et al., 2013
¹² CH ₄	soil	n/a	n/a	1	Snover and Quay, 2000
¹³ CH ₄	OH	1.0039	$2.44 \times 10^{-12} \times e^{\frac{-1775}{T}}$	n/a	Burkholder et al., 2019
¹³ CH ₄	Cl	1.06	$9.057 \times 10^{-12} \times e^{\frac{-1360}{T}}$	n/a	Feilberg et al., 2005
¹³ CH ₄	soil	n/a	n/a	1.0670	Snover and Quay, 2000



Table A1. Sites that are included in the *in situ* inversions. All sites are part of the NOAA network, other than KRS, which is part of the JR-STATION network, monitored by NIES Japan.

Code	Full Name	Latitude	Longitude
ALT	Alert Station	82.28	-62.30
ZEP	Ny-Alesund, Svalbard	78.90	11.89
SUM	Summit, Greenland	72.60	-38.42
BRW	Barrow Station	71.32	156.61
ICE	Storhofdi,Iceland	63.40	-20.29
KRS	Karasevoe, Siberia	58.14	82.25
MHD	Mace Head, Ireland	53.33	-9.90
SHM	Shemya Island, Alaska	52.71	174.12
UUM	Ulaan Uul, Mongolia	44.45	111.09
NWR	Niwot Ridge, Colorado	40.05	-105.59
UTA	Wendover, Utah	39.90	-113.72
WLG	Mt. Waliguan, China	36.29	100.90
BMW	Bermuda	32.26	-64.88
WIS	Ketura, Israel	29.96	35.06
IZO	Izana, Tenerife	28.31	-16.50
MID	Midway Islands	28.22	-177.37
KEY	Key Biscane, Florida	25.67	-80.16
ASK	Assekrem, Algeria	23.26	5.63
KUM	Cape Kumukahi, Hawaii	19.56	-154.89
MLO	Mauna Loa, Hawaii	19.54	-155.58
RPB	Ragged Point, Barbados	13.17	-59.43
SEY	Mahe Island, Seychelles	-4.68	55.53
ASC	Ascension Island	-7.97	-14.40
SMO	American Samoa	-14.25	-170.56
CGO	Cape Grim	-40.68	144.69
BHD	Baring Head	-41.40	174.87
CRZ	Crozet Island	-46.43	51.85
USH	Ushuaia, Argentina	-54.84	-68.31
PSA	Palmer Station, Antarctica	-64.77	-64.05
SYO	Syowa Station, Antarctica	-69.01	39.59
SPO	South Pole, Antarctica	-89.98	-24.8